ISWI School 2012
Puncak, Indonesia
September 20, 2012

Ionosphere irregularities

Mamoru Yamamoto
RISH, Kyoto University, Japan

Contents

- Concentrate on the low-latitude ionosphere.
- Vertical coupling of the Earth's atmosphere.
- 1st topic: Equatorial Spread-F (Plasma bubble)
  - ➢ Observations and phenomena
  - ➢ Growth rate, seeding mechanisms, etc.
- 2nd topic: Irregularity in the E-region
  - ➢ Two-stream and gradient-drift instability
  - ➢ Phenomena in mid-latitude ionosphere

Text book

M. C. Kelley with R. A. Heelis, The Earth's Ionosphere: Plasma Physics and Electrodynamics (International Geophysics Series), Academic Press, San Diego, October 1989.

(2nd edition of May 2009 is available: ISBN-13 978-0120884254)

Space Weather and Earth's influence

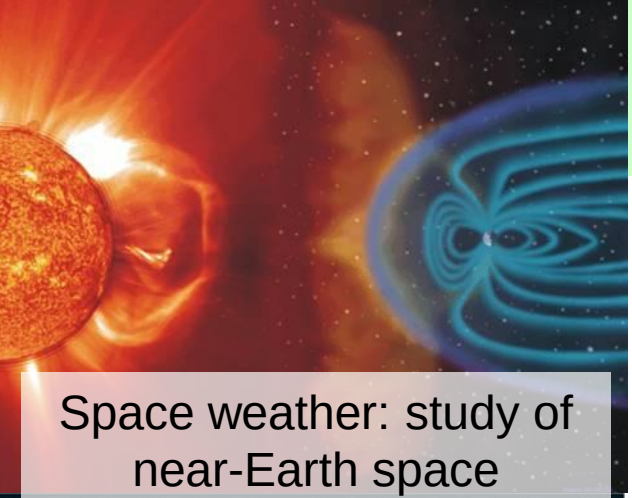

Space weather: study of near-Earth space environment

Ionosphere is the height range for ISS and Space Shuttle

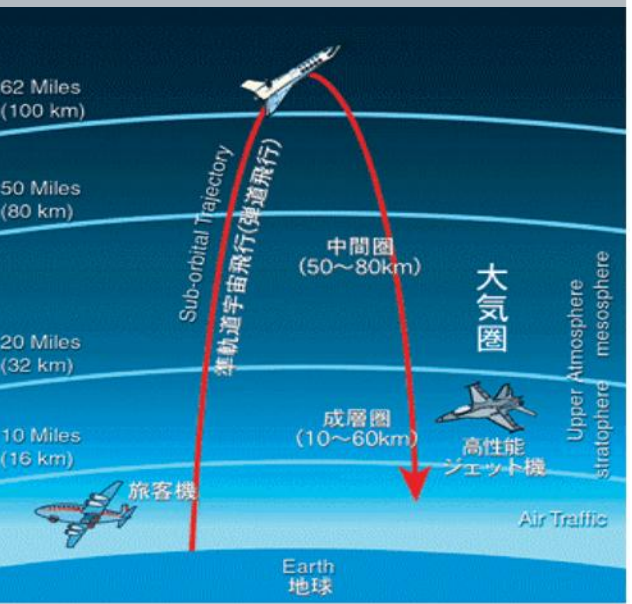

Space weather is a program to observe, assess, and forecast the space environment, which is very important for constant operation of satellite systems and reliable communication / navigation purposes.

Not only the study of the Sun-to-Earth system, but also studies of vertical coupling of the atmosphere / ionosphere is important. Regional observations (especially in the low latitudes) are thus necessary.

Ionosphere (about 300km high)

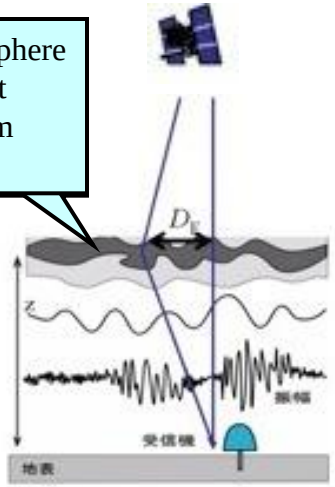

Satellite signal is scintillated by the disturbance of the ionosphere.

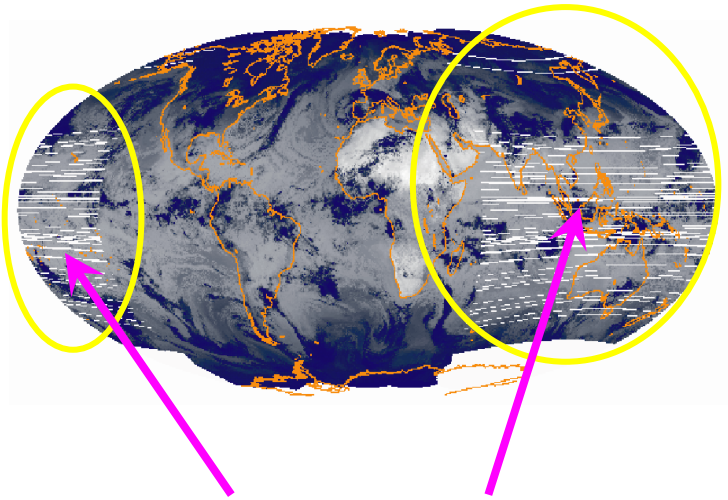

Noisy data transform from meteorological satellites only occurs over Asia.

Atmosphere waves generated by convection activities

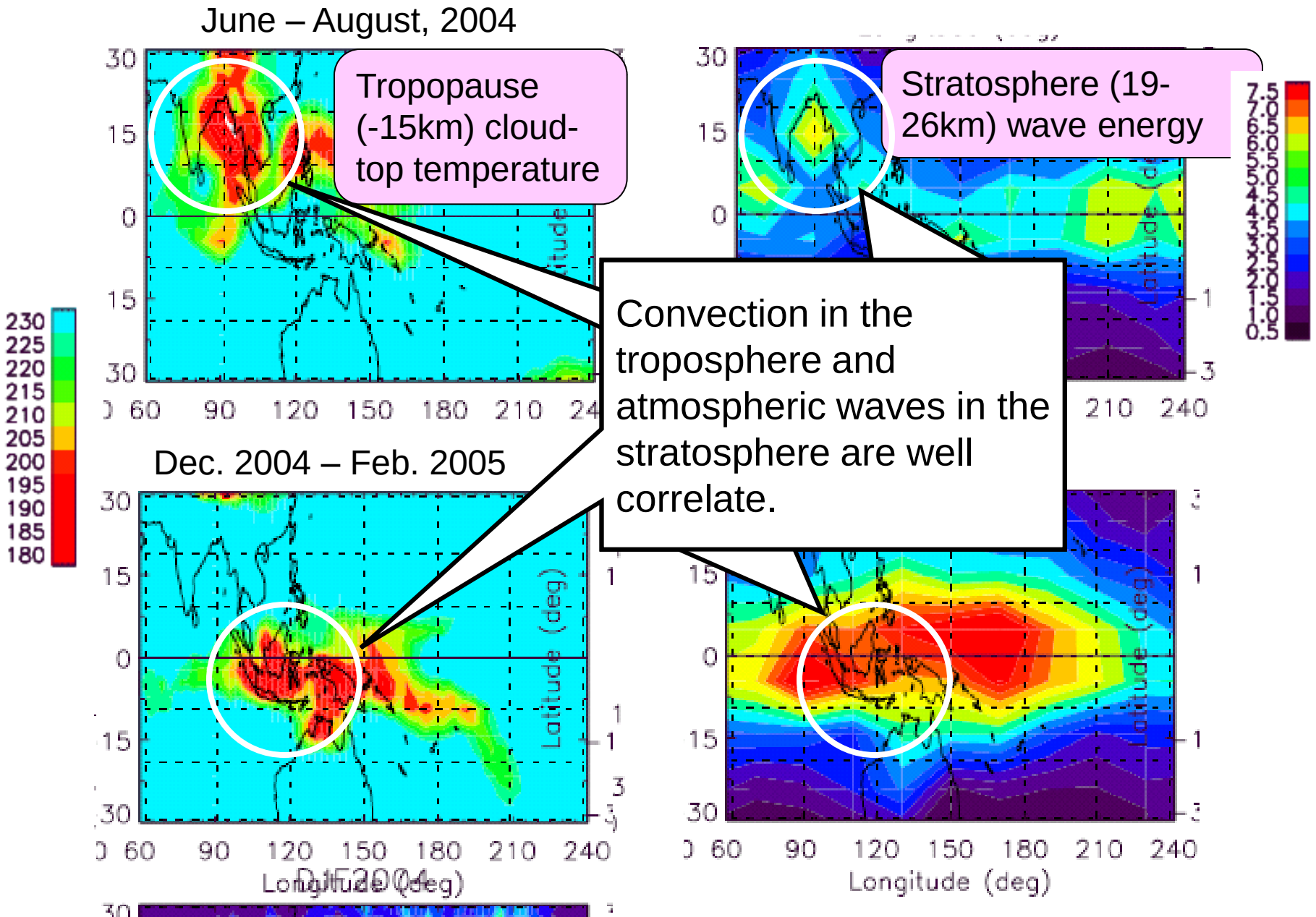

Stratospheric QBO and mesospheric SAO show intensive correlation

(another vertical coupling with atmospheric waves)

Mesosphere 86–94km

Zonal wind: MF radar in Tirunelveli, India

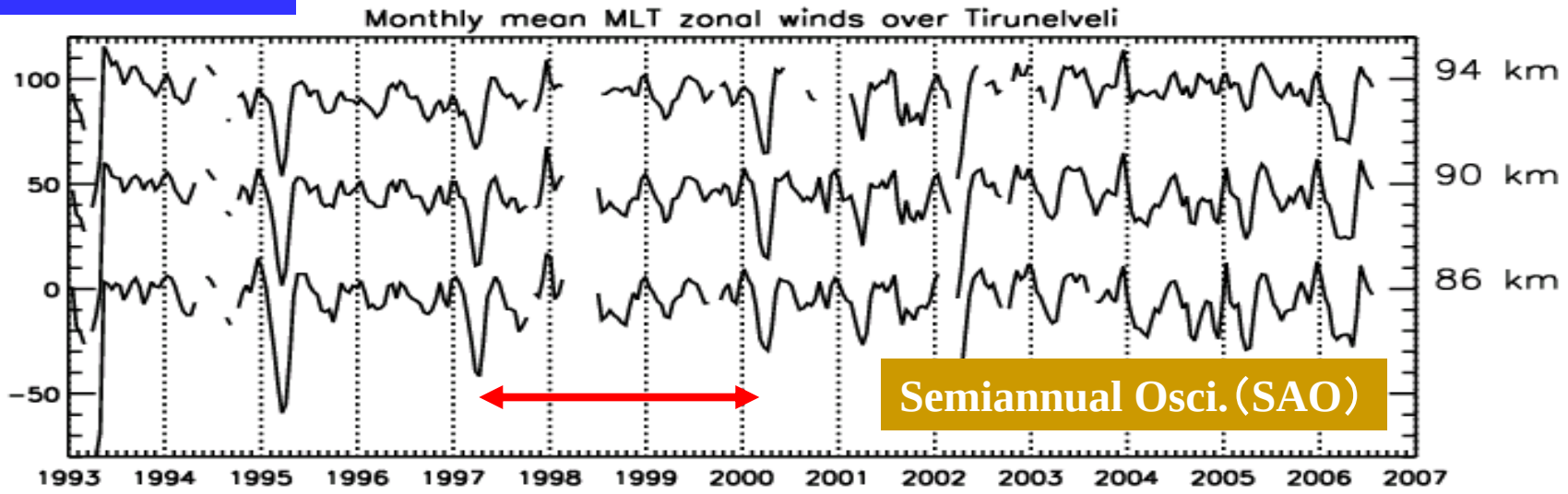

Stratosphere 20–40km

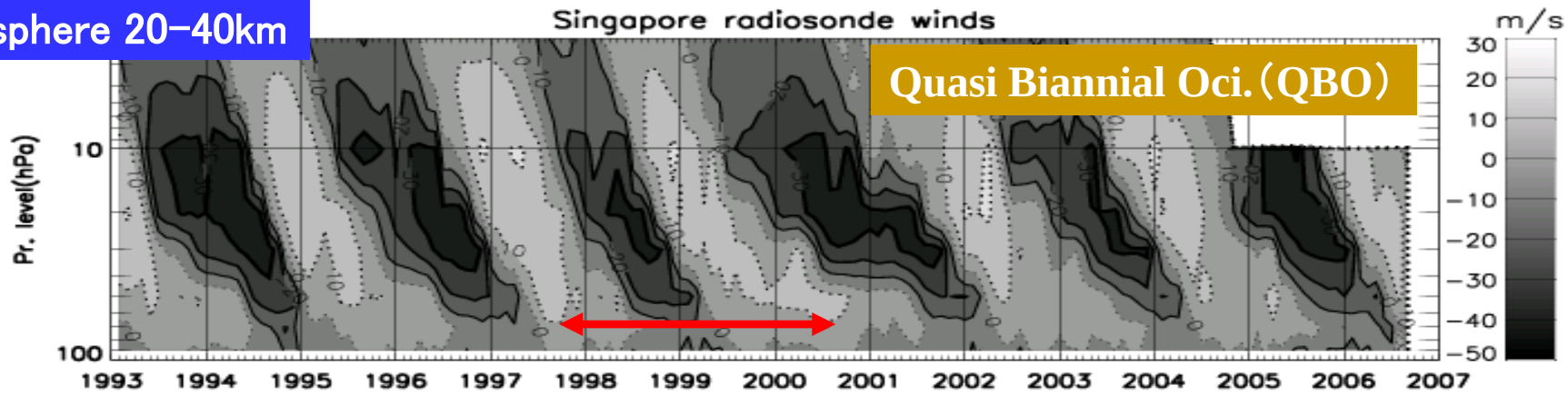

Zonal wind: Radiosonde at Singapore

Effect of lower atmosphere to the region of space weather

Atmospheric density at 400km altitutde

Distribution of land/sea

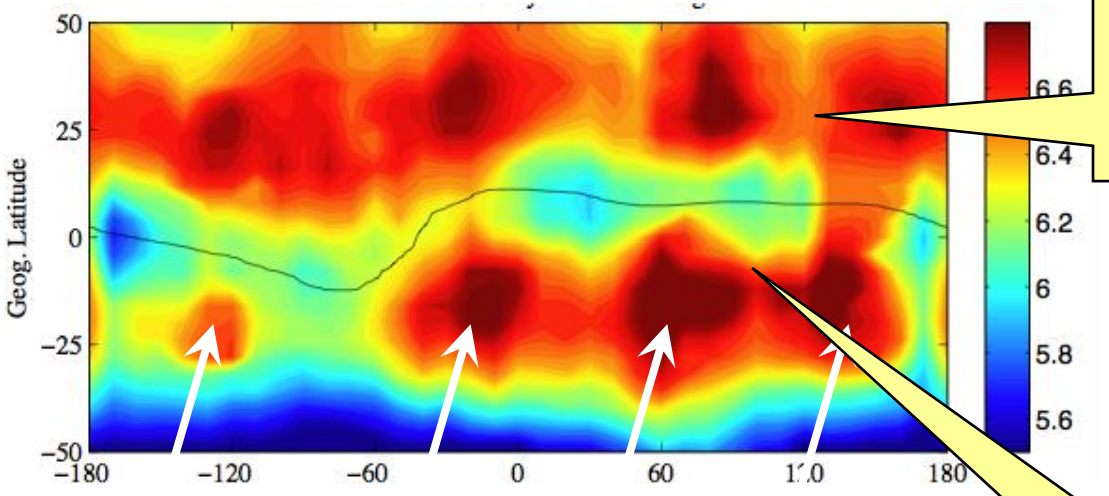

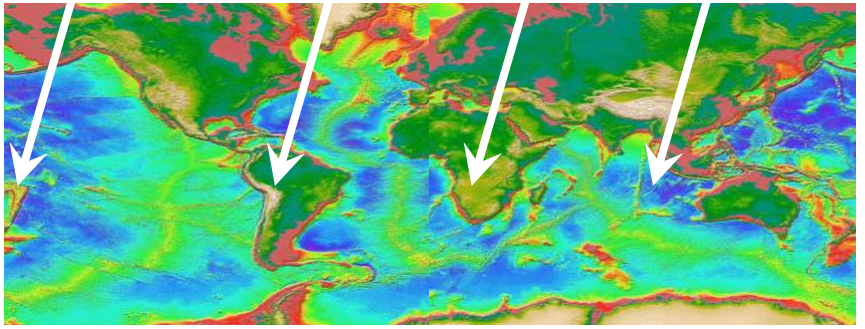

Okinawa (Japan)
Lat.: 26N
Mag. Lat.: 16N

Similarity

Jakarta
(Indonesia)
Lat.: 6S
Mag. Lat.: 16S

○Atmospheric density at satellite height show latitudinal patter that resembles to the Earth's land/sea distribution
→Regional study is important in the space weather studies.
○South of Japan and Jakarta are in similar geomagnetic latitudes.

VHF Radars in the Low-Latitude Region

dip equator

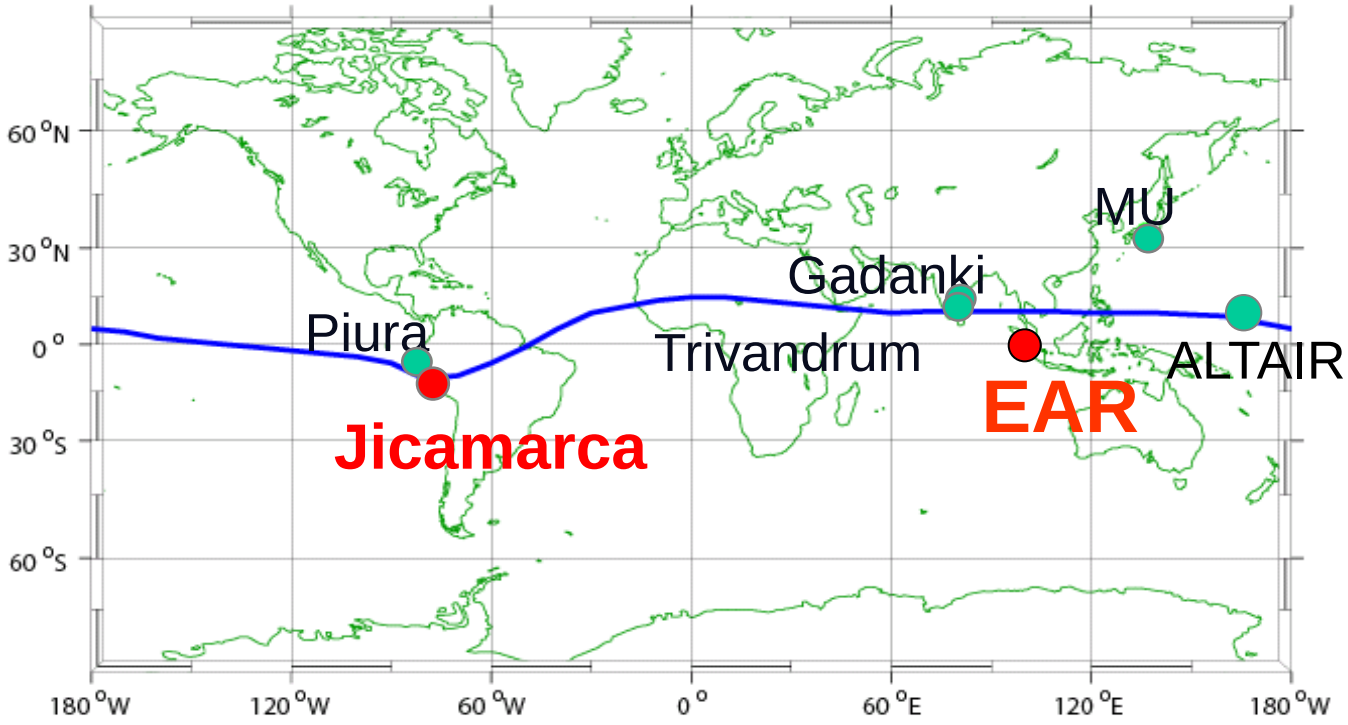

※EAR: Equatorial Atmosphere Radar
(located right at the geographic equator and in the geomagnetic southern hemisphere)

Jicamarca radar in Peru

赤道域の電離圏・熱圏に特有のユニークなプラズマ過程がこのレーダーにより解明されてきた.

50 MHz, 2 MW, 300 m x 300 m アレーアンテナ

Equatorial Atmosphere Radar (EAR)

Antenna field (110m in diameter)

Located at Kototabang,
West Sumatra,
Indonesia
(0.20° S, 100.32° E)

Operated since 2001 under close collaboration between RISH and LAPAN

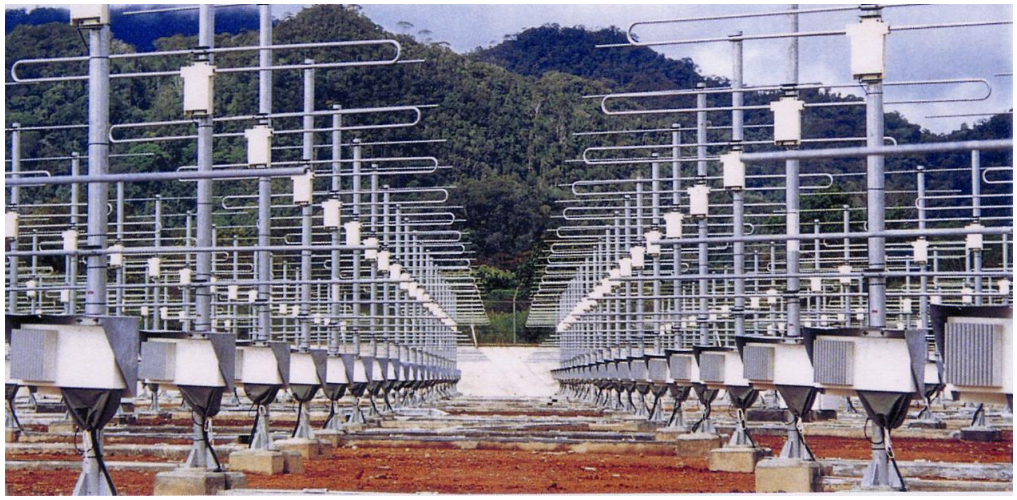

47MHz, 100 kW, 560 Yagi antennas

F-region dynamo in evening

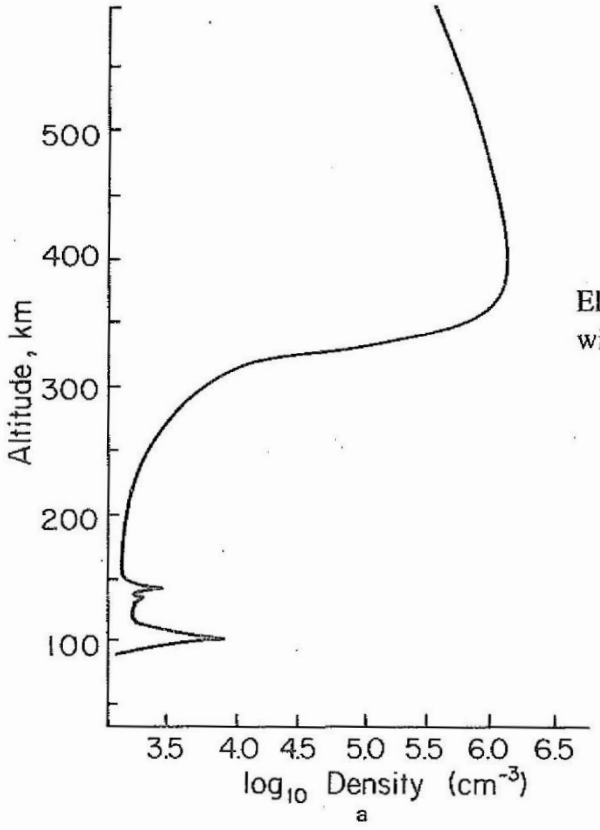

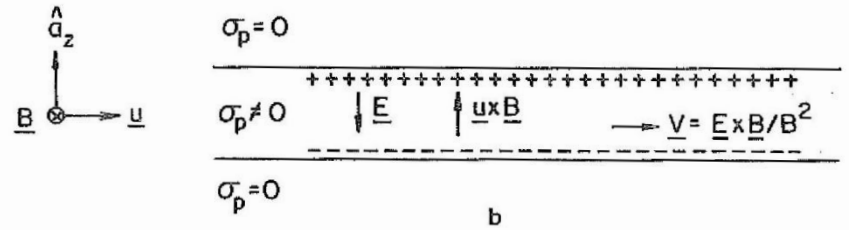

Fig. 3.8. (a) Typical equatorial plasma density profile in the evening local time period. (b) Electrodynamics of the equatorial F region, in which the density and conductivity profile is modeled with a slab geometry, subject to a constant zonal eastward neutral wind.

Neutral wind in the evening is naturally eastward (with large variability). This sets positive/negative charges at the top/bottom side of F-region. (Governing condition is $J_z = 0$)

Vertical drift of equatorial ionosphere

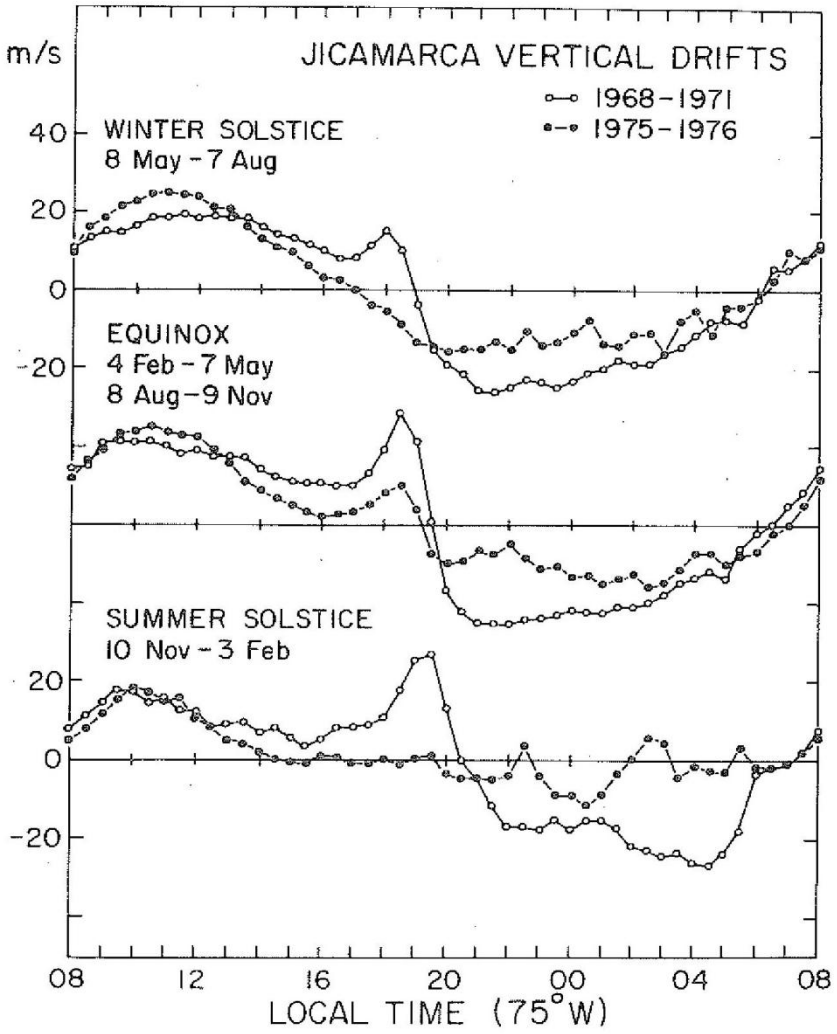

Fig. 3.2. Same as Fig. 3.1 but for the vertical drift component, which is positive for motions upward. [After Fejer *et al.* (1979). Reproduced by permission of the American Geophysical Union.]

Pre-reversal enhancement (PRE) /Post sunset rise (PSR) mechanism

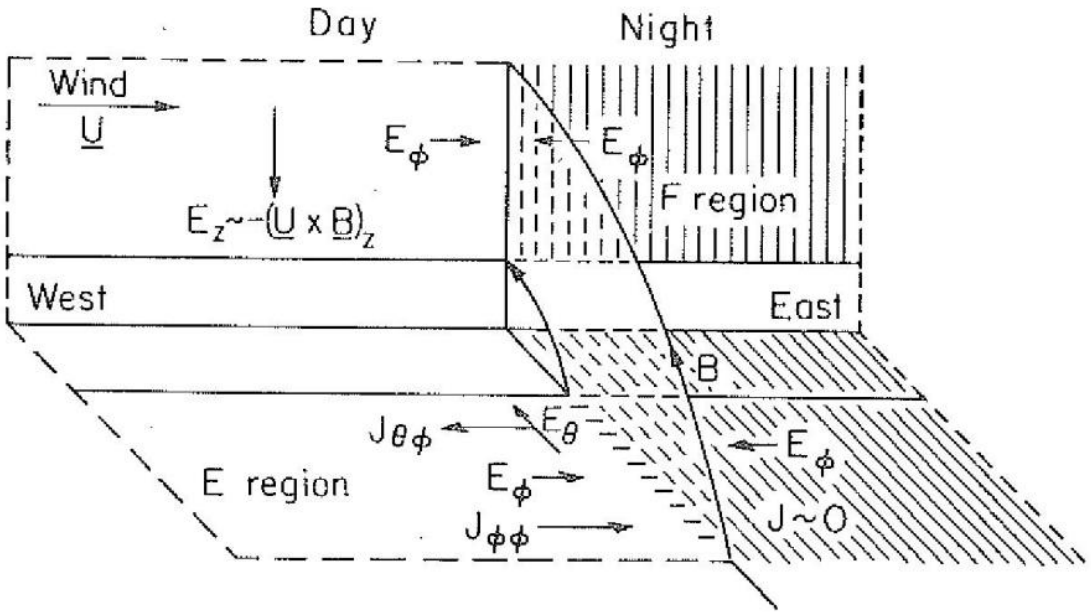

Fig. 3.19. Simplified model of the F-region prereversal enhancement driven by a uniform F-region wind **U**. Near the sunset terminator the F-region dynamo E_z is no longer shorted out and approaches $-\mathbf{U} \times \mathbf{B}$. This field maps to an equatorward E_θ in the E layer and drives a westward Hall current $J_{\theta\phi}$. But if no current flows in the nightside E region, a negative polarization charge must develop at the terminator, with E_ϕ as shown and $J_{\phi\phi}$ canceling $J_{\theta\phi}$. This E_ϕ maps back to the F region and causes first an upward (day) and then a downward (night) $\mathbf{E} \times \mathbf{B}$ plasma drift. [After Farley *et al.* (1986). Reproduced with permission of the American Geophysical Union.]

1st topic: Equatorial Spread-F (ESF)

Jicamarca VHF radar obs.

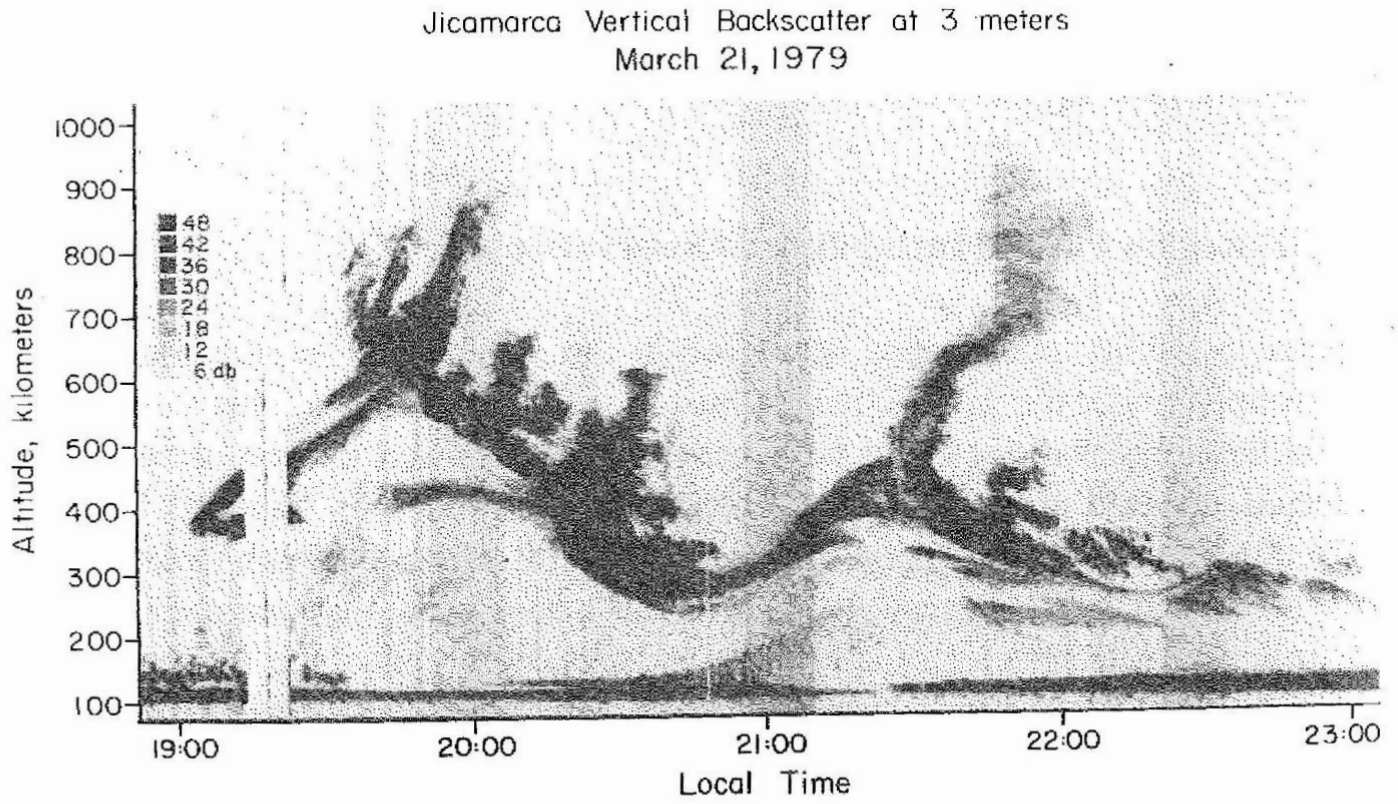

Fig. 4.1. Range–time–intensity map displaying the backscatter power at 3-m wavelengths measured at Jicamarca, Peru. The gray scale is decibels above the thermal noise level. [After Kelley *et al.* (1981). Reproduced with permission of the American Geophysical Union.]

F-region Field Aligned Irregularity (FAI) Echoes from the EAR

Altitude-Time Intensity (ATI) plot

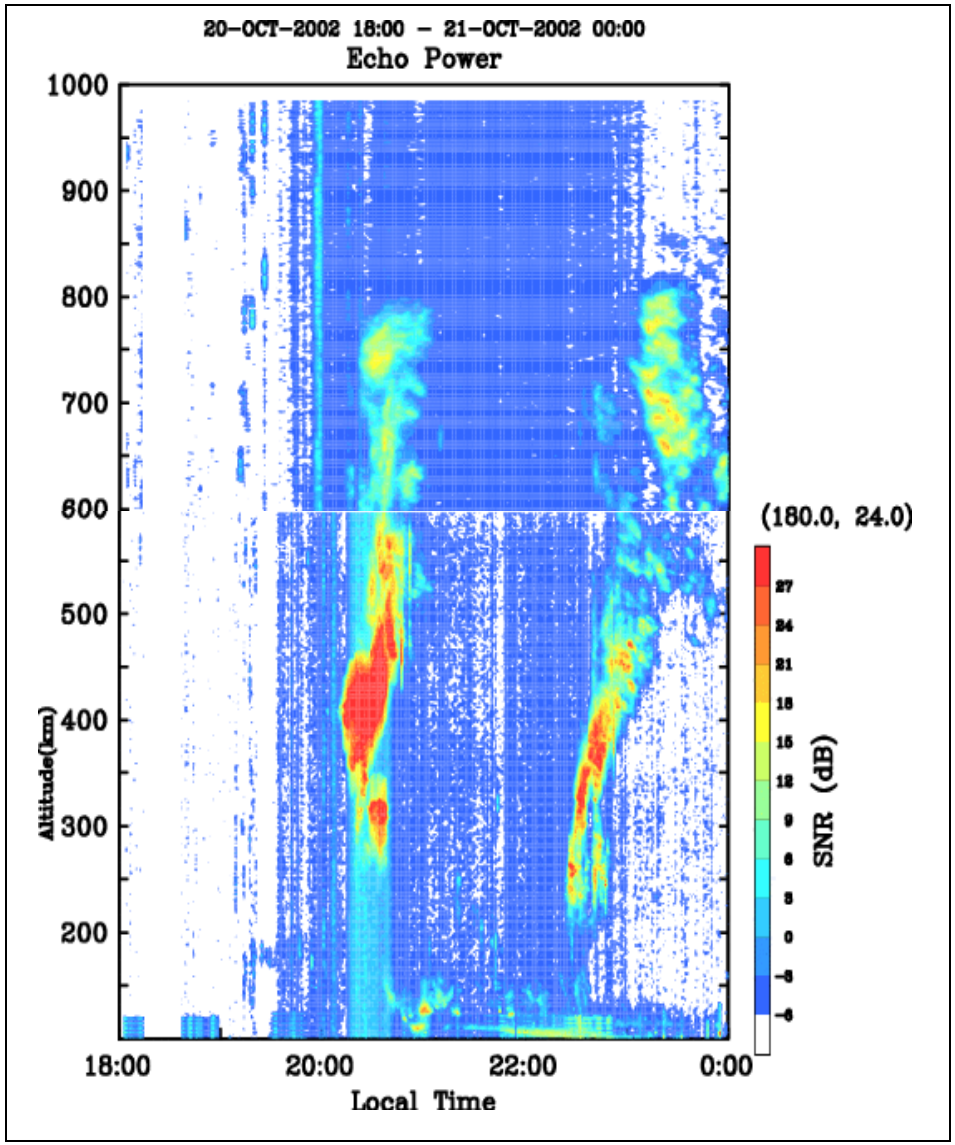

Intense FAI echoes associated with plasma bubbles were observed from the EAR southward beam soon after the F-region sunset. Maximum altitude of the echoes reached 800 km.

S. Fukao, Y. Ozawa, T. Yokoyama, M. Yamamoto, and R. T. Tsunoda, *J. Geophys. Res.*, **109**, A02304, 2004.

Kototabang (EAR)
March 18, 2011

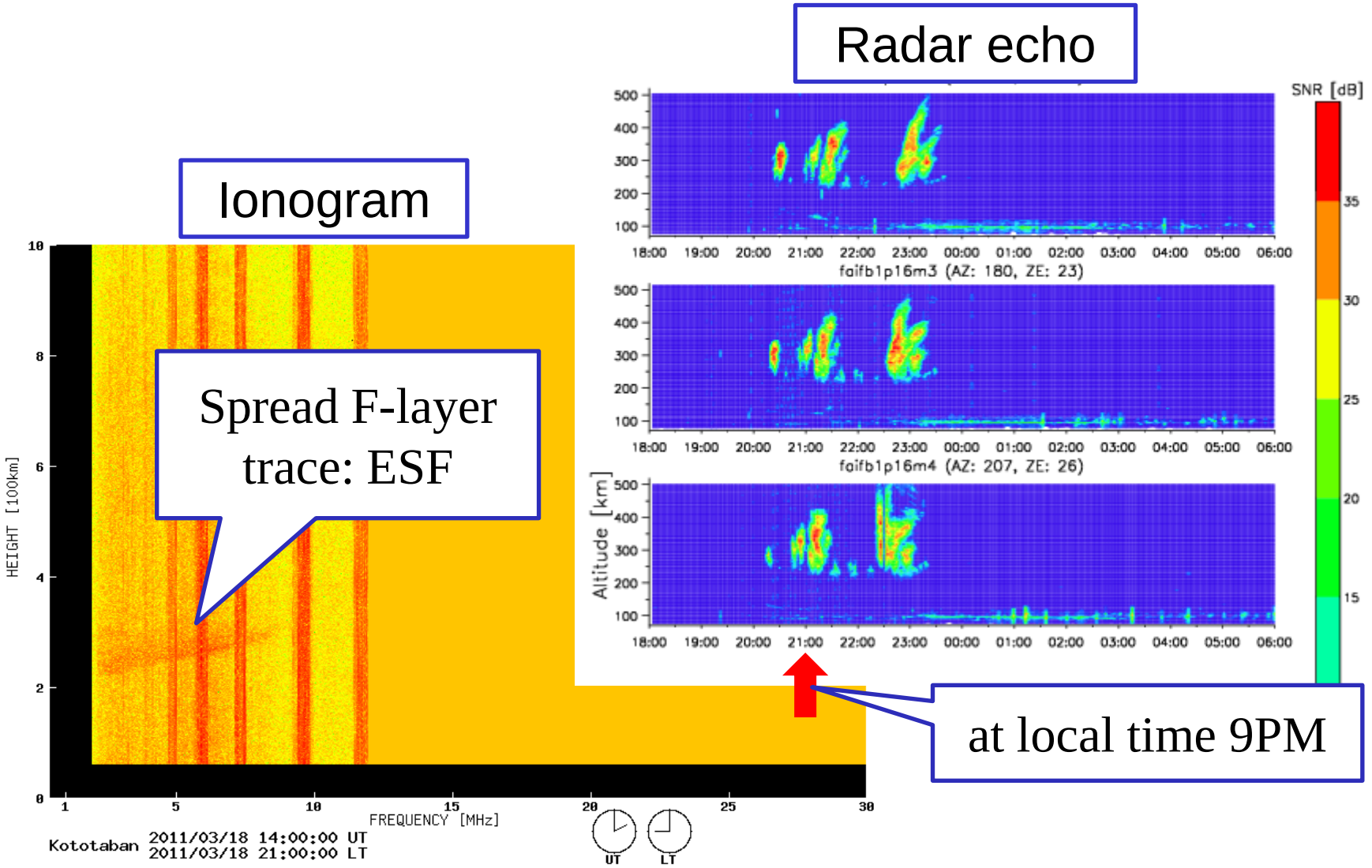

ESF occurrence just after the sunset
(EAR results from Fukao et al., 2004)

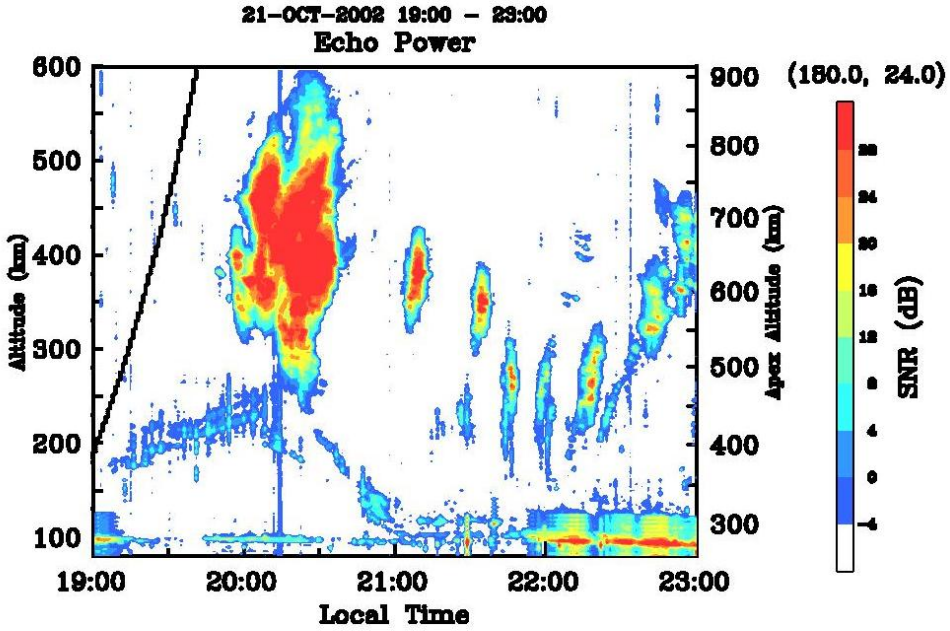

Figure 5. ATI plot for backscatter from the FAI observed in Beam 6 (to the south) from 1900 to 2300 LT on October 21, 2002. The thick solid curve shows the solar terminator.

EAR Multiple Beam Observation of ESF

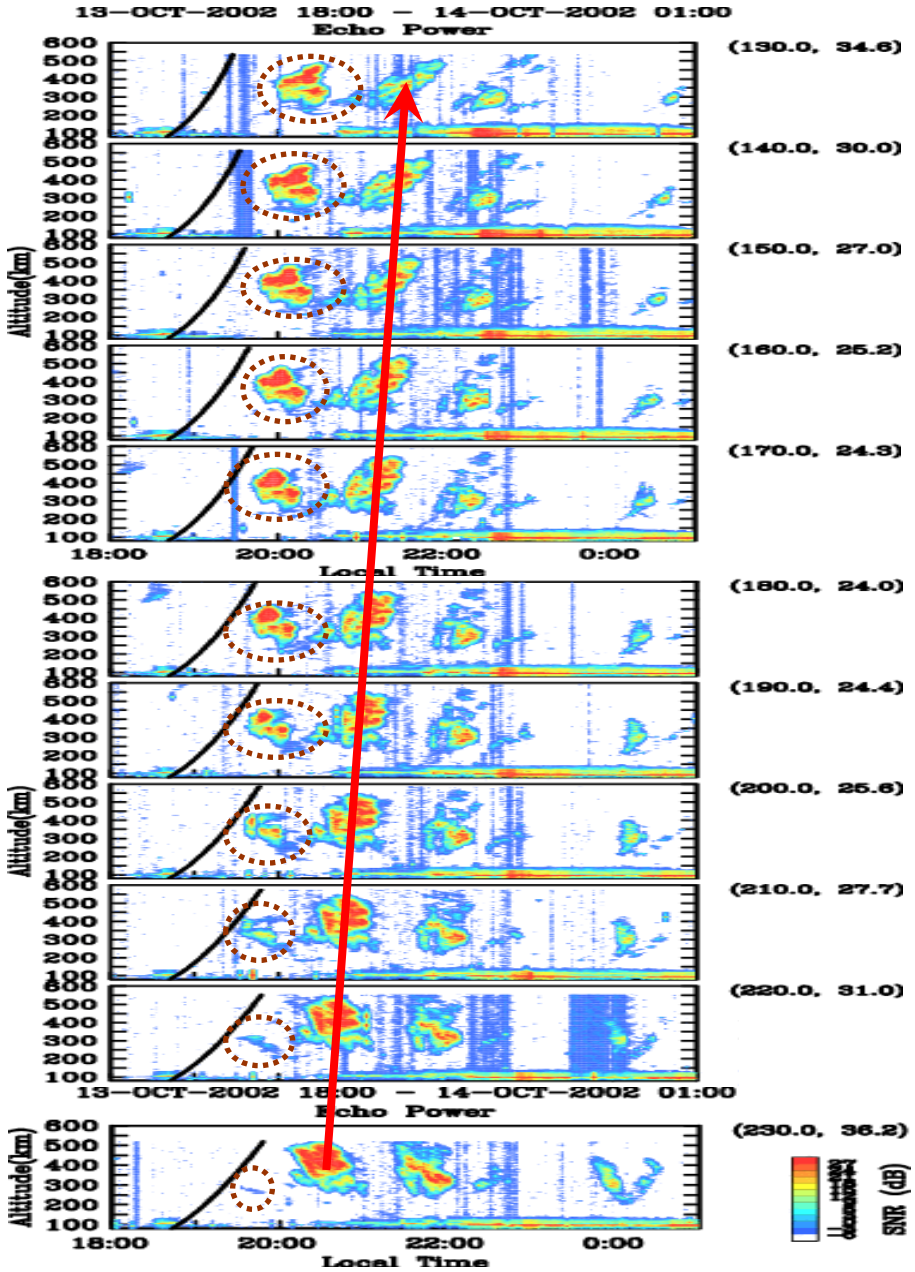

EAST

SOUTH

WEST

Growing FAI

Growing FAIs were detected in the observation region with 11 beam directions.

Eastward propagation of FAI echoing region is clearly seen.

Terminator

Motion of zonal structure of plasma bubbles observed by EAR

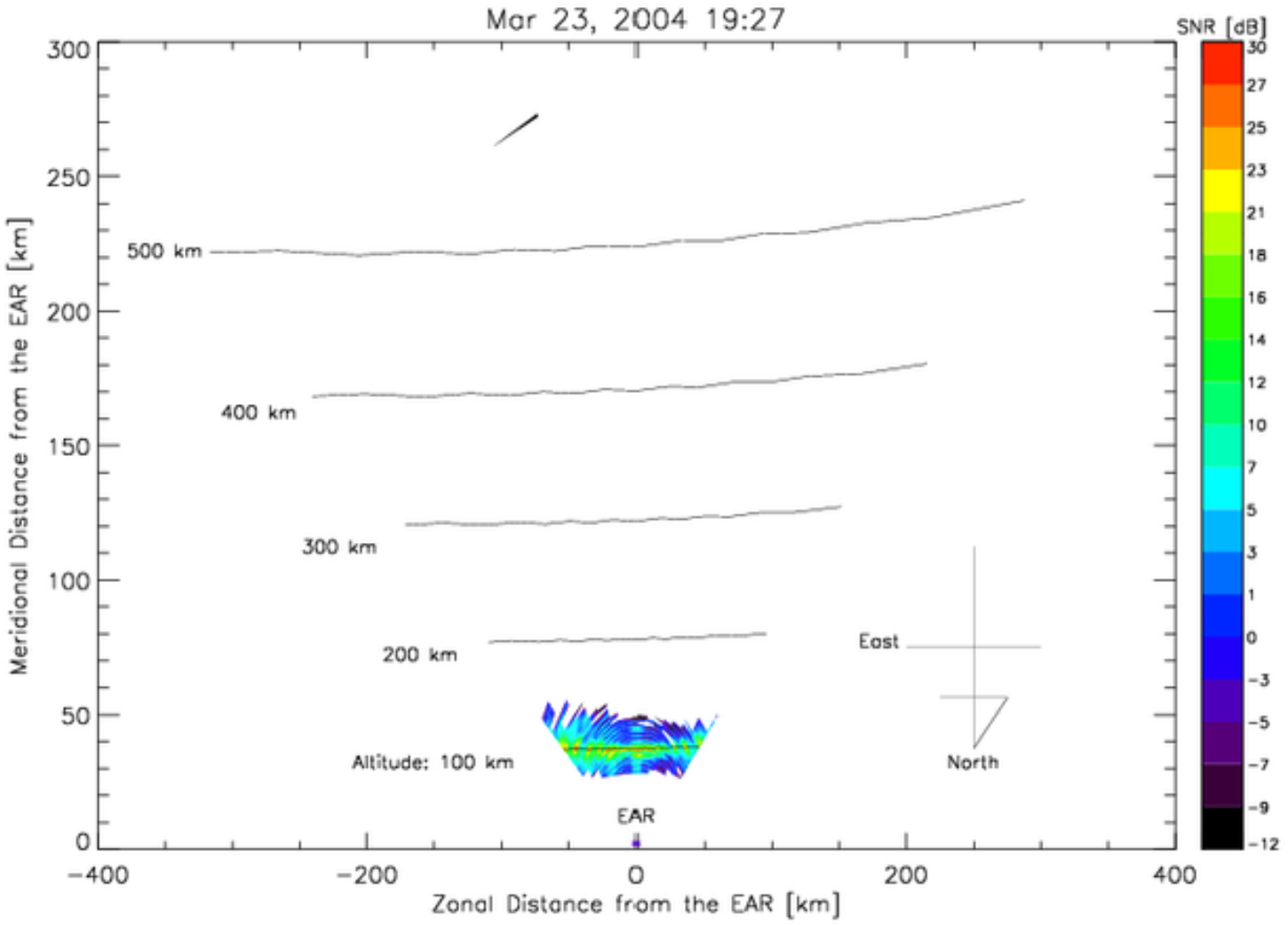

ESF and density depletion

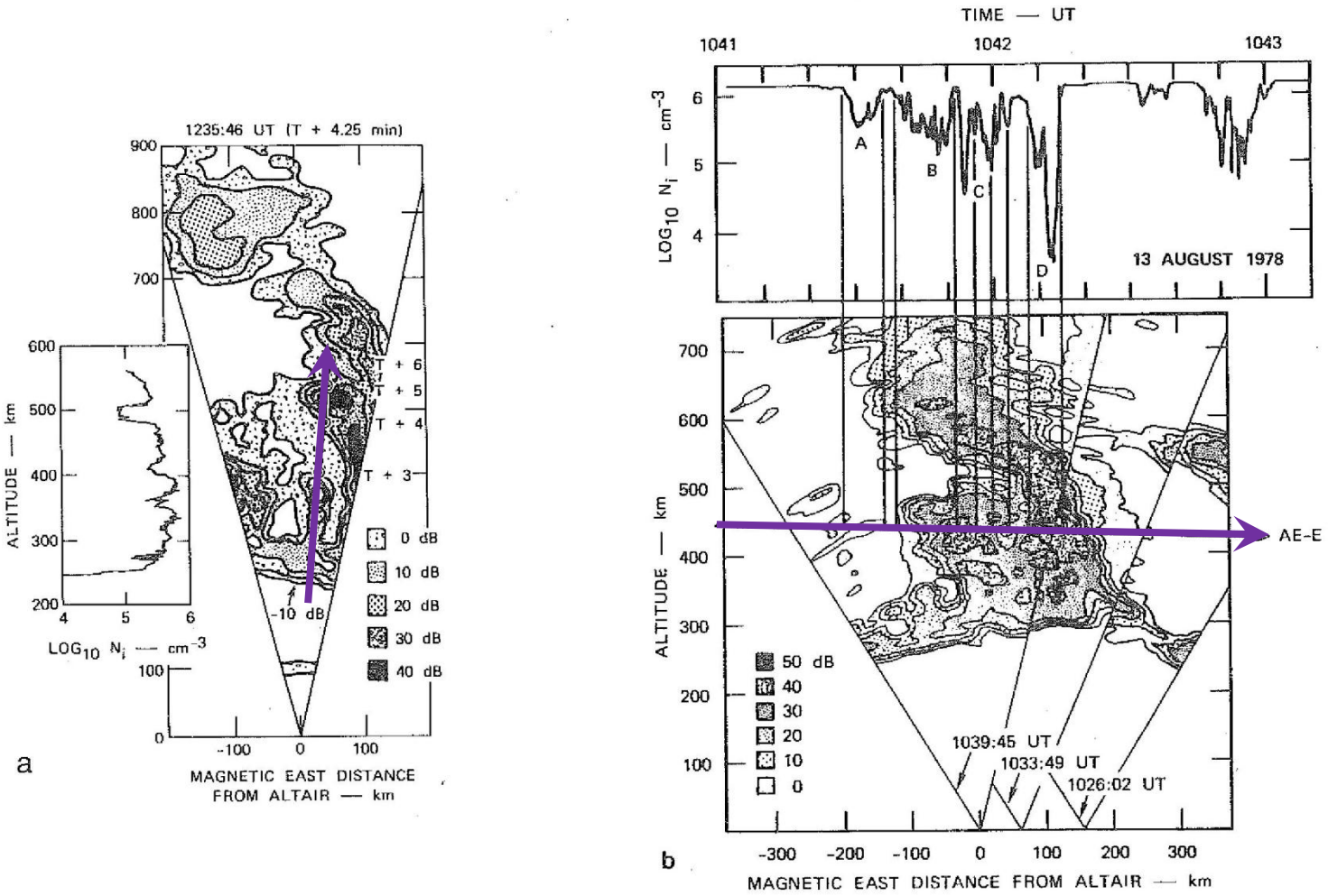

Fig. 4.3 (a) Simultaneous vertical rocket plasma density profile and backscatter map made with the Altair radar on the island of Kwajalein. Dots show the rocket trajectory. [After Rino *et al.* (1981) Reproduced with permission of the American Geophysical Union.] (b) Simultaneous horizontal satellite plasma density profile and backscatter map made with the Altair radar. [After Tsunoda *et al* (1982). Reproduced with permission of the American Geophysical Union.]

Dynamic spectrum of ESF density

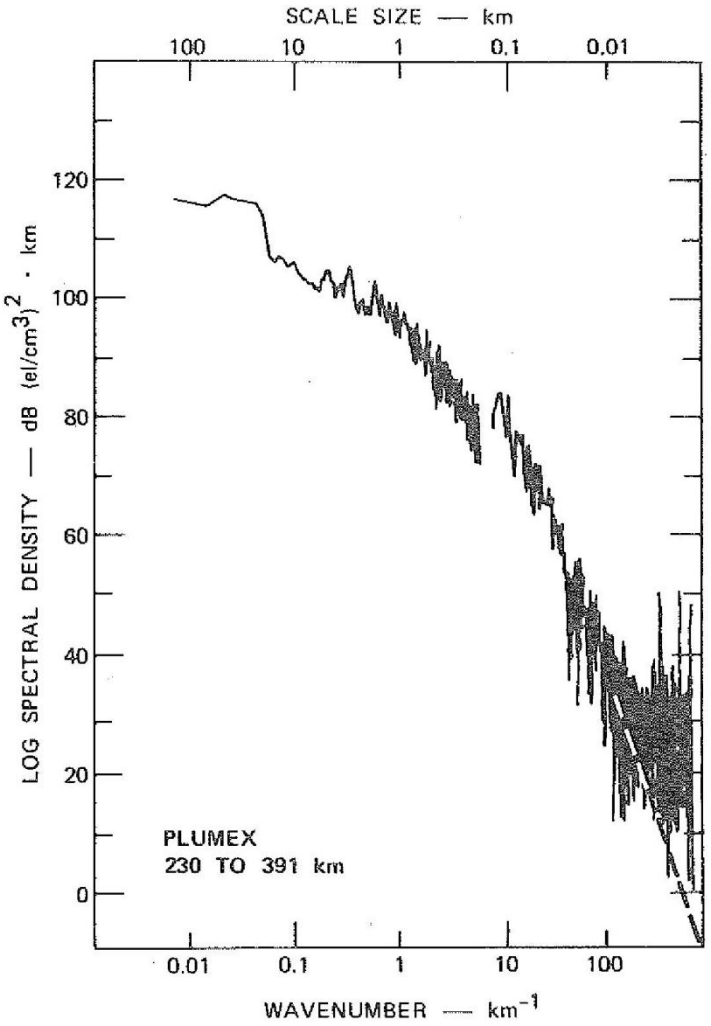

Fig. 4.5. Power spectrum of the plasma density detected along the rocket trajectory shown in Fig. 4.3. Note that wave number here actually means inverse wavelength which equals $k/2\pi$. [After Kelley *et al.* (1982). Reproduced with permission of the American Geophysical Union.]

Plasma Bubbles Observed with Airglow Imagers at Conjugate Points

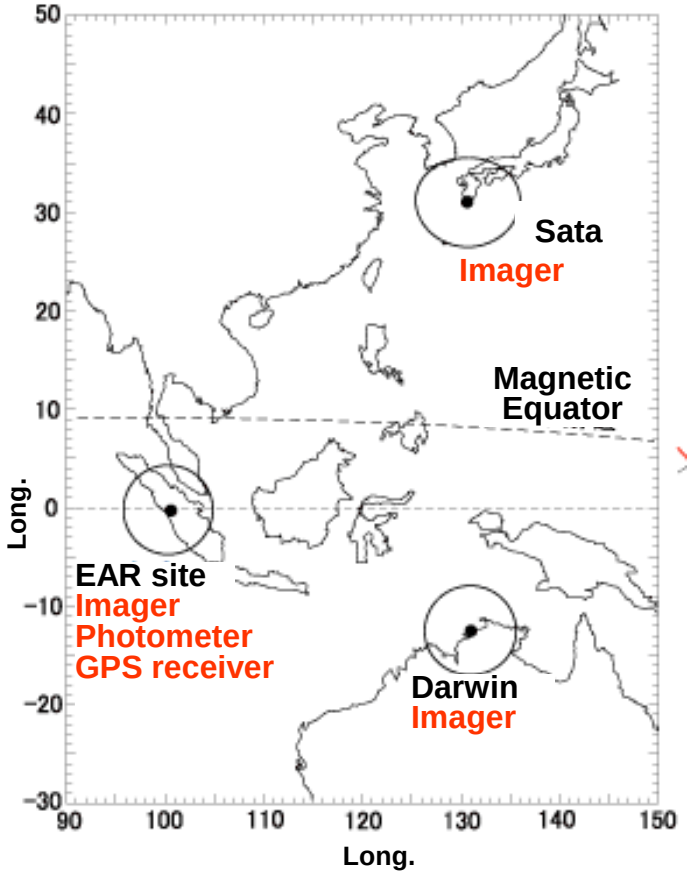

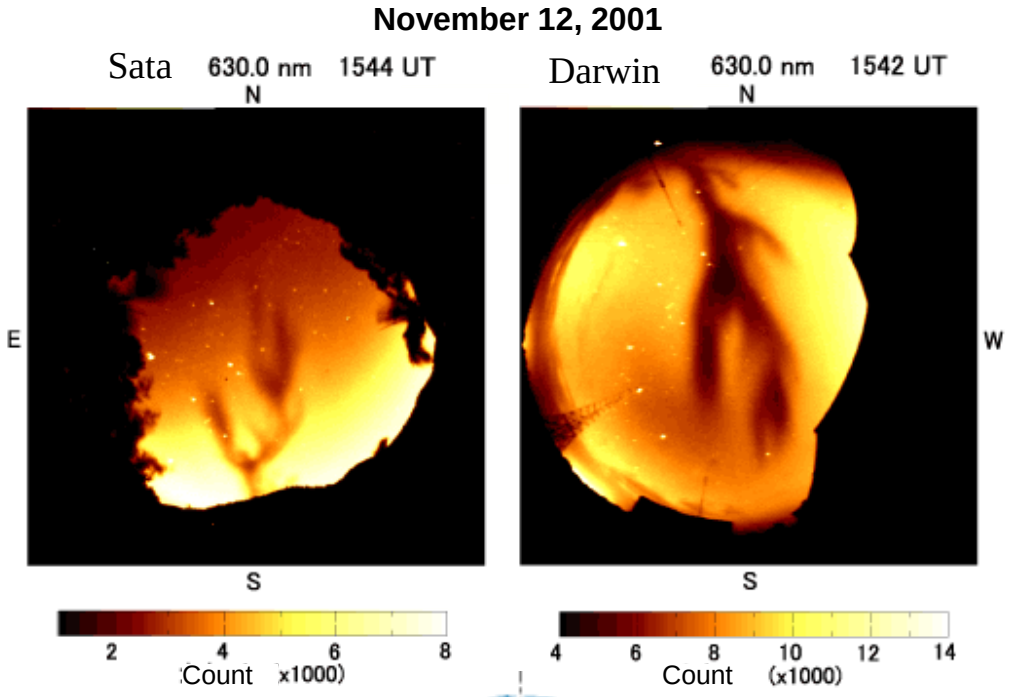

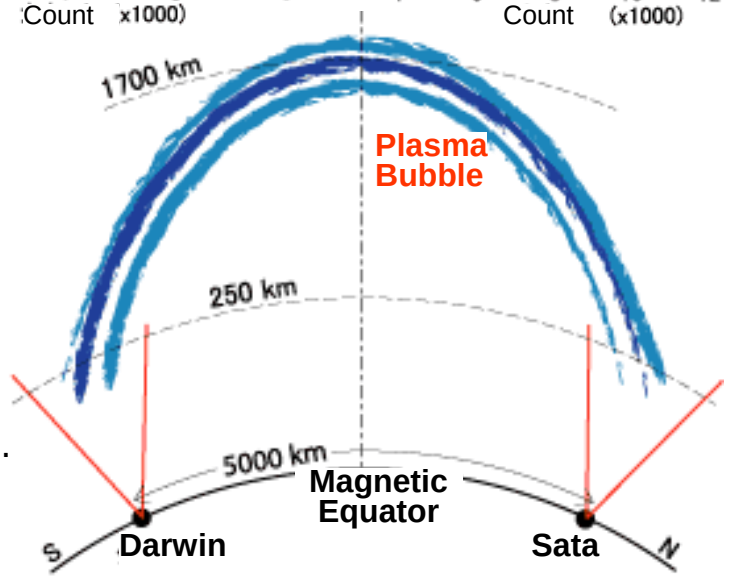

Observation by Prof. Ogawa group
STE Lab., Nagoya Univ.

Otsuka, Y., K. Shiokawa, T. Ogawa, and P. Wilkinson, *Geophys. Res. Lett.*, 29(15), 10.1029/2002GL015347, 2002.
Shiokawa, K., Y. Otsuka, T. Ogawa, and P. Wilkinson, *Ann. Geophysicae*, in press, 2004.

Equatorial Spread-F (ESF)

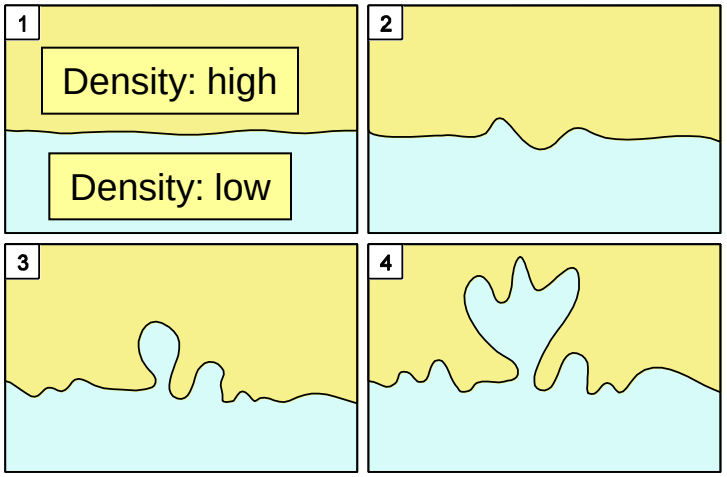

Development of plasma bubbles

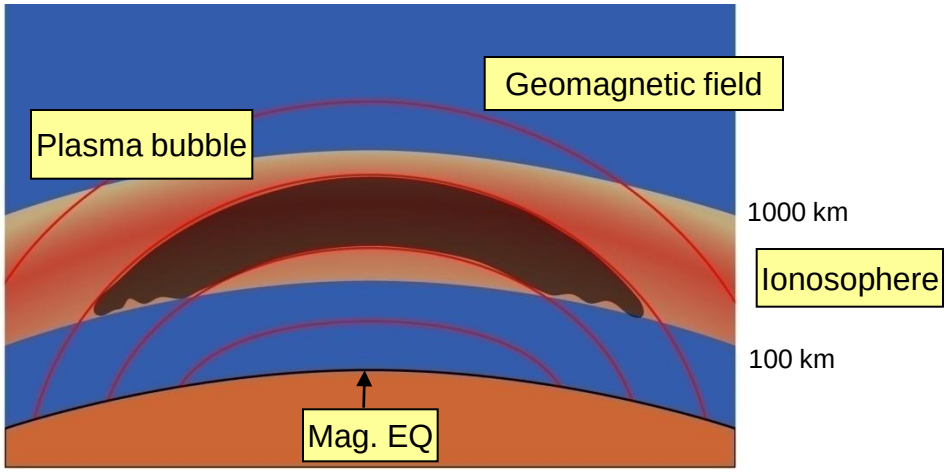

Meridional structure of plasma bubbles

- Local density-depleted regions at the bottomside of the ionosphere develop and rapidly move upward to the topside of the ionosphere.
- Rayleigh-Taylor instability is the mechanism.
- ESF occurs mainly near F-region sunset over the magnetic equator.
- Meridionally elongated structure along the field line.
- Accompanied with small-scale irregularities that are detectable by VHF radars.

Concept of Rayleigh-Taylor instability

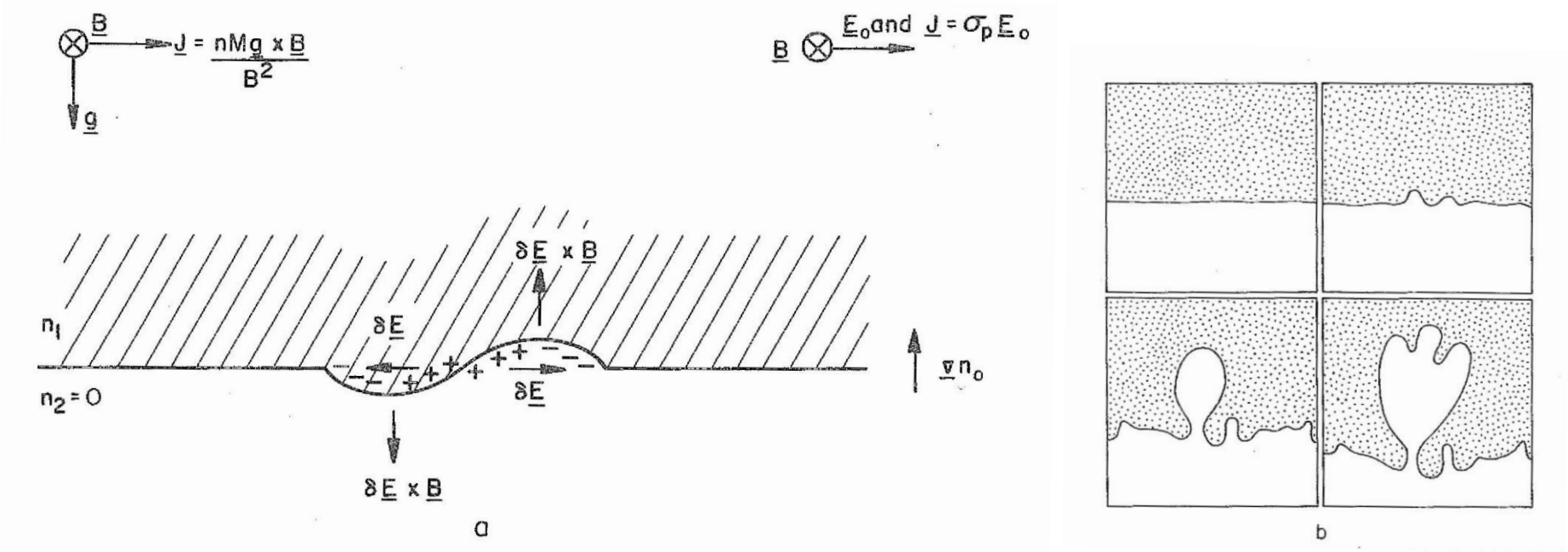

Fig. 4.8. (a) Schematic diagram of the plasma analog of the Rayleigh–Taylor instability in the equatorial geometry. (b) Sequential sketches made from photos of the hydrodynamic Rayleigh–Taylor instability. A heavy fluid is initially supported by a transparent lighter fluid.

Theory of ESF

- ESF is considered as Rayleigh-Taylor instability occurring at the bottomside of the F-region. Governing equations are,

$$\frac{\partial n}{\partial t} + \mathbf{V} \cdot \nabla n = 0 \,(\text{Fluid continuity for electron and ion})$$

$$\nabla \cdot \mathbf{J} = 0 \,(\text{Current continuity})$$

  where n, t , $\boldsymbol{V}$, are density, time, and velocity vector. $\boldsymbol{J}=\boldsymbol{V_i}$ - $\boldsymbol{V_e}$ is current vector.

- Generation of the polarization electric field *E'* is essential for stability of the plasma.

Theory of ESF

- Linear growth rate of R-T instability is then,

$$\gamma_{\mathrm{RT}} = \frac{\mathbf{g}}{\nu_{\mathrm{in}} L} + \frac{E_{x0}}{LB}$$

where

$\mathbf{g}$: gravity, ν_{in} : ion - neutral collision, E_{x0} : eastward electrid field

B : geomagneti c field, n_0 : background p lasma density,

$$L = \left(\frac{1}{n_0} \frac{dn_0}{dz} \right)^{-1} : \text{Scale length of the density gradient}$$

R-T instability is unstable by gravity (term 1) and ambient eastward electric field (term 2).

- Term 1 shows that small collision (= high ionosphere) is favorable for the instability.
- Term 2 shows that electric field by storm initiates ESF.
- R-T instability may be generated by eastward or downward component of the neutral wind.

Occurrence and variability of ESF

ESFs mainly occur after the local sunset preiod. This is explained by post-sunset rise (PSR, or pre-reversal enhancement (PRE)) that is the electromagnetic behavior of the ionosphere at the sunset terminator. If so, why ESF show large day-to-day variability. Large-Scale Wave Structure (LSWS) is considered as a key to this problem.

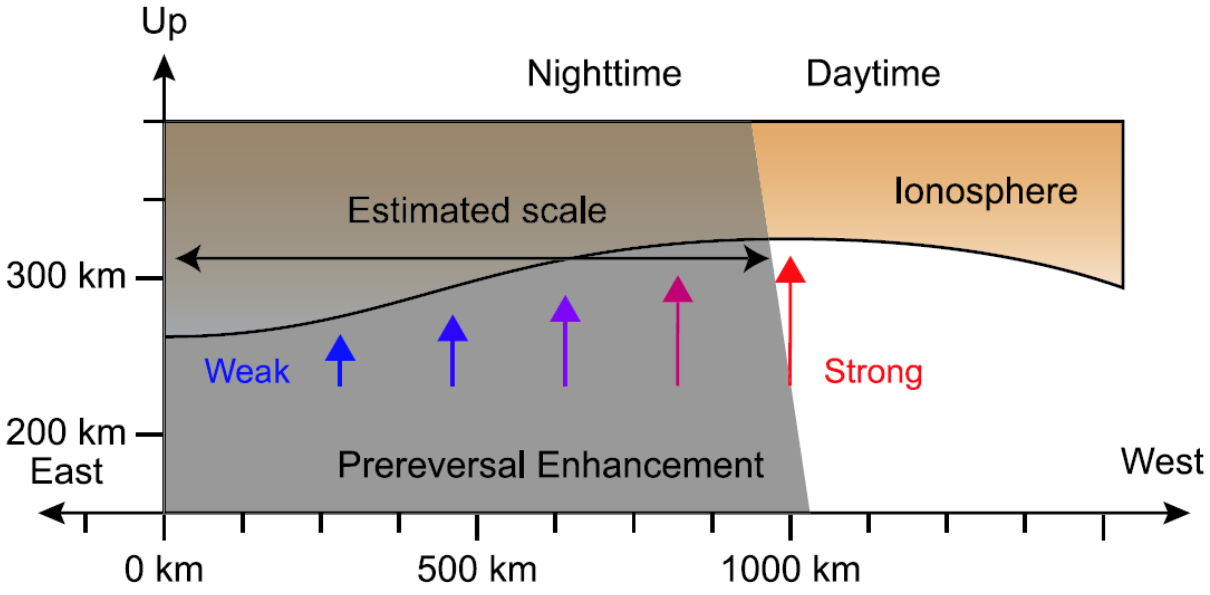

Fukao et al., 2006

LSWS measured with 630nm imager
(Makela et al, GRL, 2010)

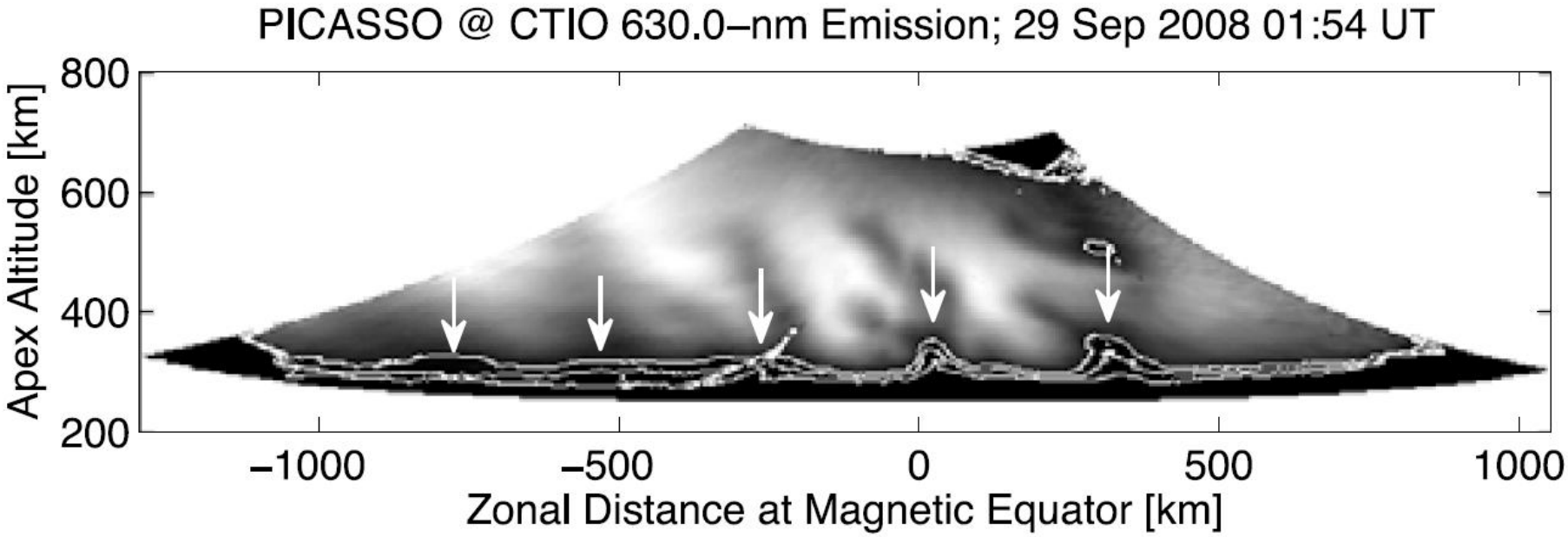

2nd topic: instabilities in the Equatorial electrojet (or E-region)

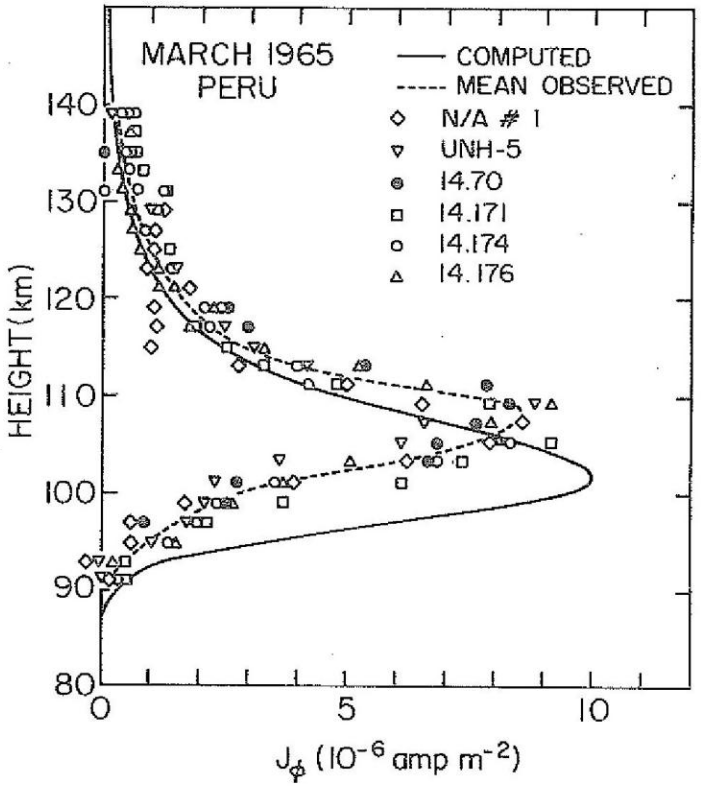

Fig. 3.16. Observed and computed eastward current density profiles near noon at the dip equator off the coast of Peru in March 1965, normalized to a magnetic field perturbation of 100 nT at Huancayo. Measured profiles are from Shuman (1970) (flight N/A #1), Maynard (1967) (flight UNH-5), and Davis *et al.* (1967) (flights 14.170, 14.171, 14.174, and 14.176). The theoretical profile is from Richmond's (1973a) theory. [After Richmond (1973b). Reproduced by permission of Pergamon Press.]

FAI in the electrojet (Type 1)

Jicamarca VHF radar obs.

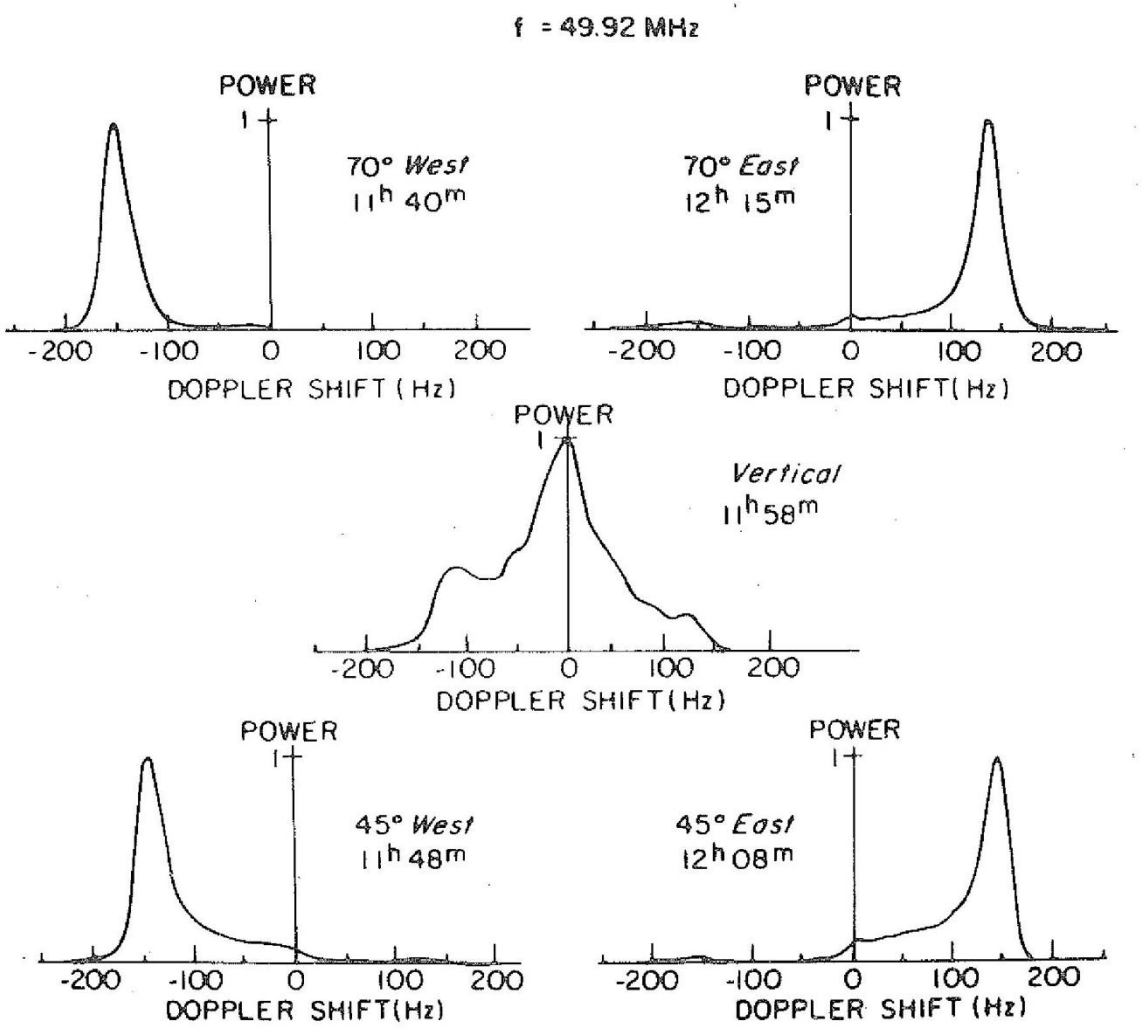

Fig. 4.20. Series of Doppler spectra from the equatorial electrojet irregularities at different elevation angles obtained at Jicamarca during a period of relatively strong scattering. The spectra are normalized to a fixed peak value. [After Cohen and Bowles (1967). Reproduced with permission of the American Geophysical Union.]

FAI in the electrojet (Type 2)

Jicamarca VHF radar obs.

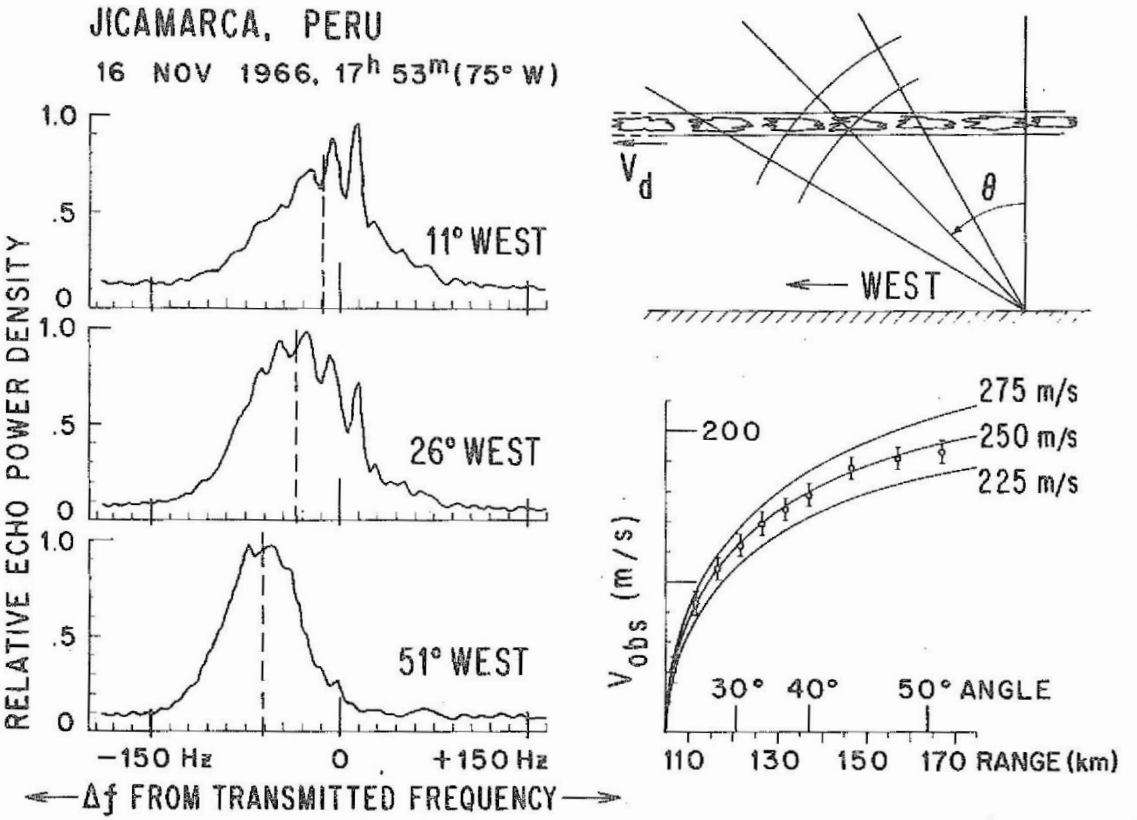

Fig. 4.21. Type 2 spectra measured at 50 MHz simultaneously at different antenna zenith angles. The dashed lines indicate the average Doppler shifts. The geometry of the experiment is shown in the top right panel. The results of the experiment, together with three theoretical curves for which a sine dependence of the average phase velocity with zenith angle was assumed, are shown in the bottom right panel. [After Balsley (1969). Reproduced with permission of the American Geophysical Union.]

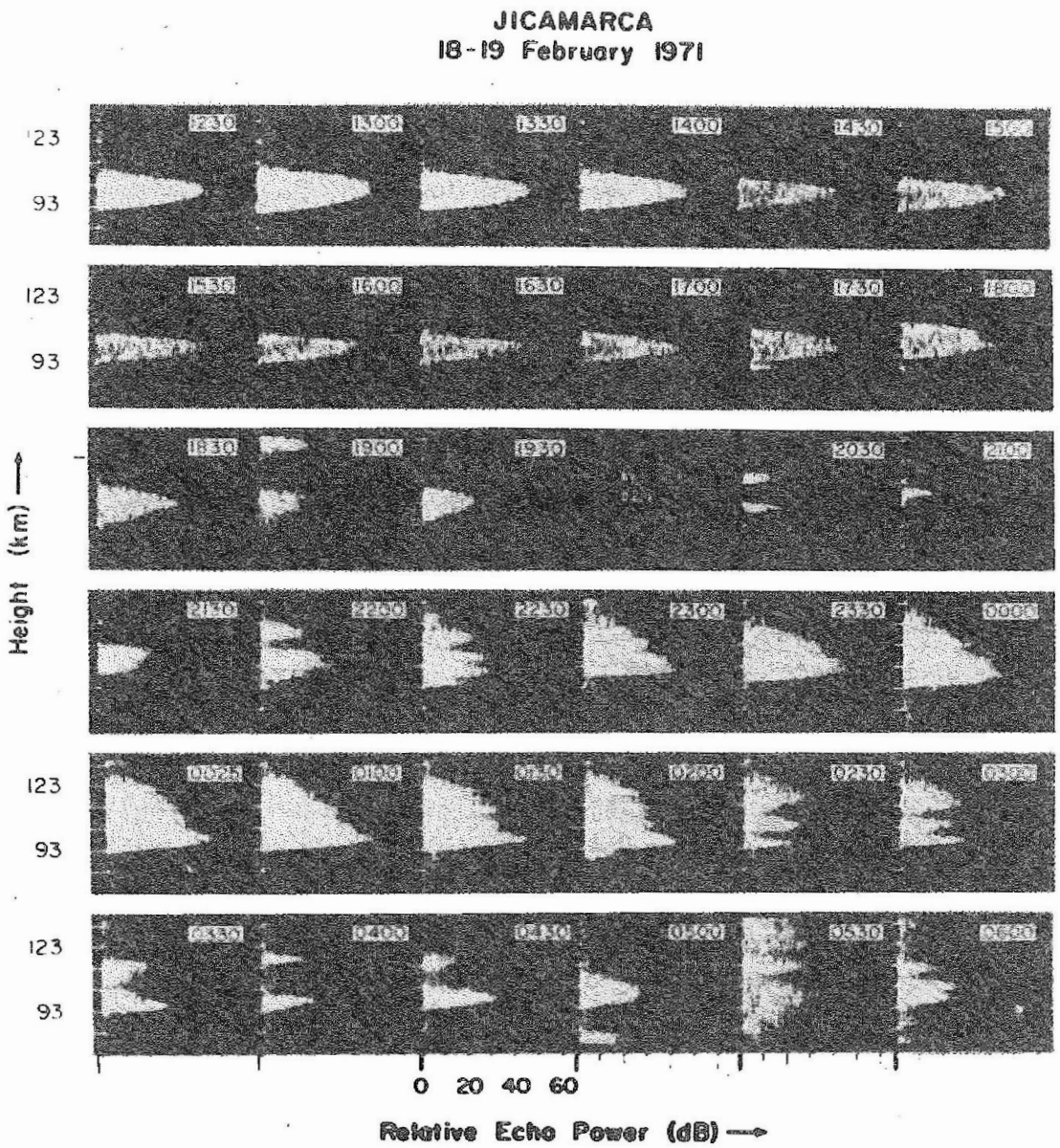

Fig. 4.23. Sample of the 50-MHz backscattering power profiles from the electrojet irregularities measured with the large vertically directed incoherent scatter antenna at Jicamarca. Spread F echoes contaminated the data between 0405 and 0550 and perhaps at 1900. [After Fejer *et al.* (1975). Reproduced with permission of the American Geophysical Union.]

Doppler shift of electrojet FAI echoes

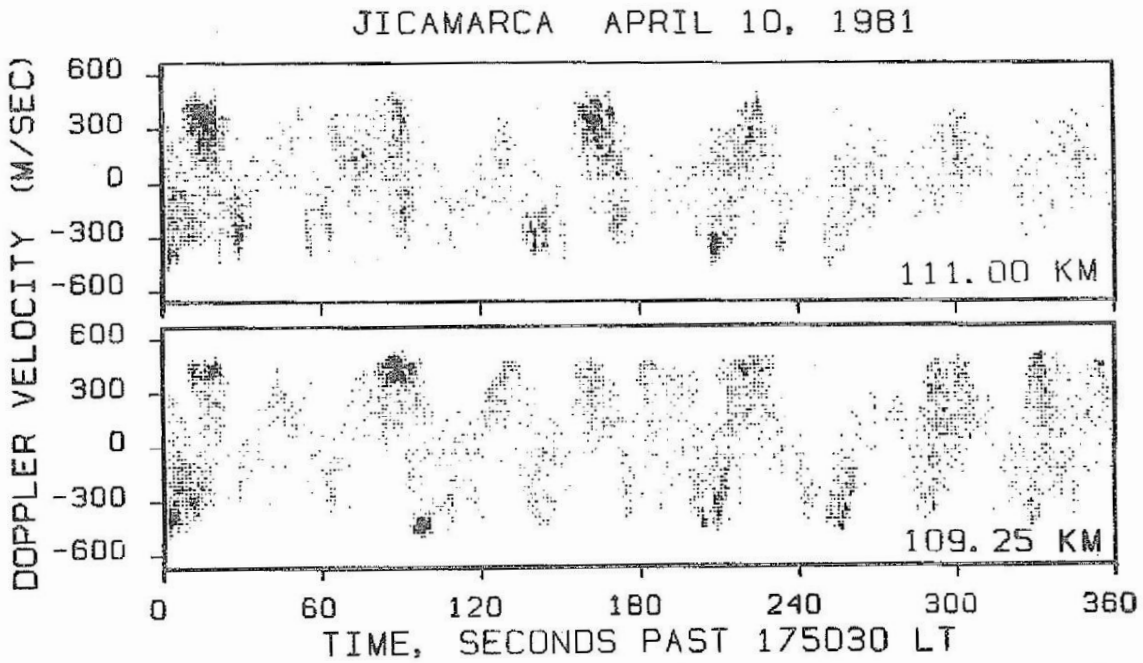

Fig. 4.24. Doppler shift spectrogram of the vertical backscatter signal measured at Jicamarca. Each spectrogram is normalized to its own peak power. The power values are divided into nine linearly spaced levels, with the darkest shades corresponding to the largest power values. Negative Doppler velocities indicate downgoing waves. [After Kudeki *et al.* (1982). Reproduced with permission of the American Geophysical Union.]

Rocket experiment of electrojet FAI

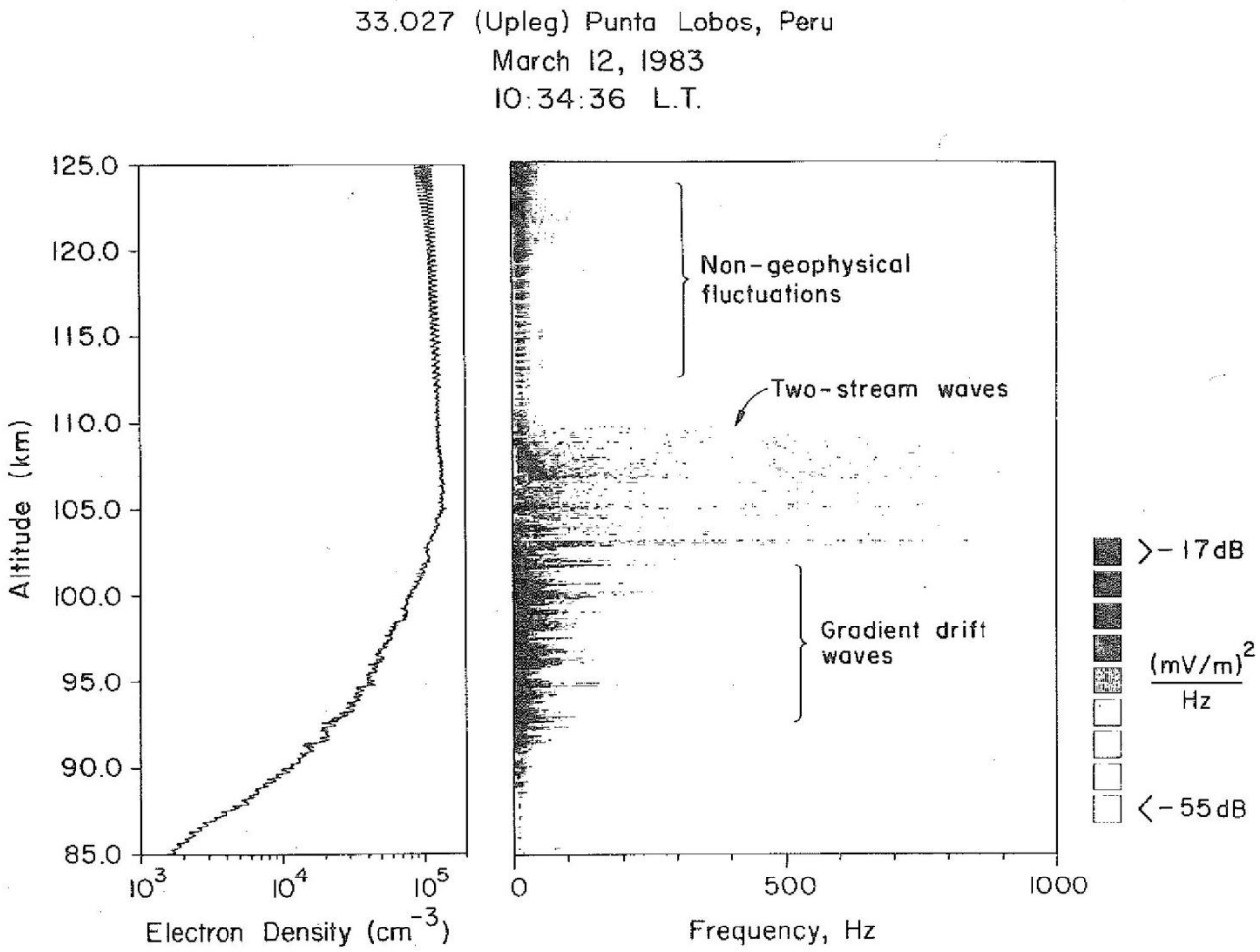

Fig. 4.27. Frequency–height sonogram of the horizontal component of the irregularities measured during the upleg of rocket 33.027 during strong electrojet conditions. This instrument had a low-frequency roll-off (3 dB) at 16 Hz. The electron density profile (left) shows the presence of large-scale irregularities. Both panels show nongeophysical "interference" above about 110 km. [After Pfaff *et al.* (1988a). Reproduced with permission of the American Geophysical Union.]

Linear theory of the E-region FAI (1)

Linear theory of E-region FAI (Fejer, et al., 1975)

Growth rate

$$\gamma = \frac{\psi}{(1+\psi)\nu_i}\left[\frac{(kV_d)^2}{(1+\psi)^2} - k^2 C_s^2\right] + \frac{V_d \nu_i}{(1+\psi)^2 \Omega_i}\frac{1}{N}\frac{dN}{dz}$$

where

k : wavenumber, $V_d = V_e - V_i$: velocity difference between electron and ion

C_s : ion sound speed, $\psi = \frac{\nu_i \nu_e}{\Omega_i \Omega_e}$: Ratio ion/electron collision to gyro frequency

From this we can infer two instabilities of two kinds.

1) Two-stream instability (related term 1 = Type 1) occurs when electrons run through ions at faster speed than the sound speed, $V_d > (1+\psi)C_s$

   This occurs mainly in the electrojet or limited conditions where intense ambient electric field apply. Radar echo show Doppler frequency $\approx C_s$

Linear theory of the E-region FAI (2)

2) Gradient-drift instability (related term 2 = Type 2) occurs when intense density gradient exists and some electric field (or neutral wind) is applied. Radar echo shows following Doppler shift of

$$V_a = \frac{1}{1+\psi}\frac{E \times B}{B^2} + \frac{\psi}{1+\psi}U_\perp$$

where $U_\perp$ is neutral wind component perpendicular to the geomagentic field. As ψ is negligible (~0) above around 100km, FAI echoes show ExB drift of plasma in the region. Below 100km consideration of the neutral atmosphere is necessary.

Linear theory of the E-region FAI (3)

(a) Two-stream instability

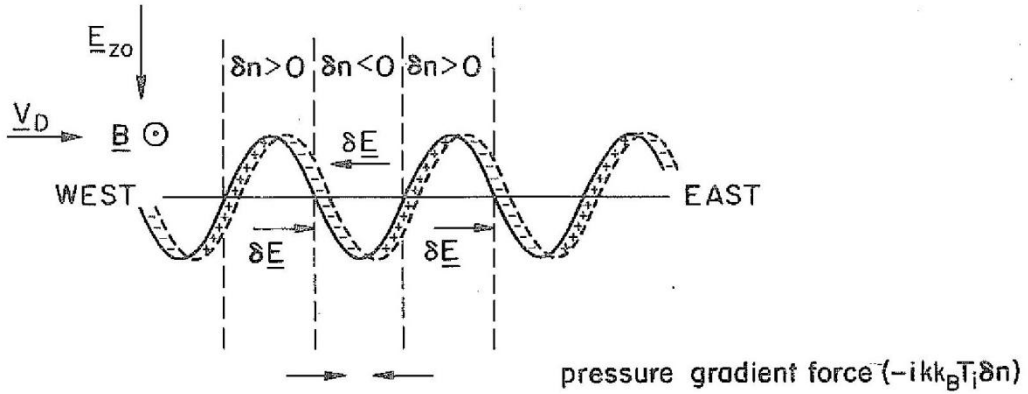

(b) Gradient-drift instability

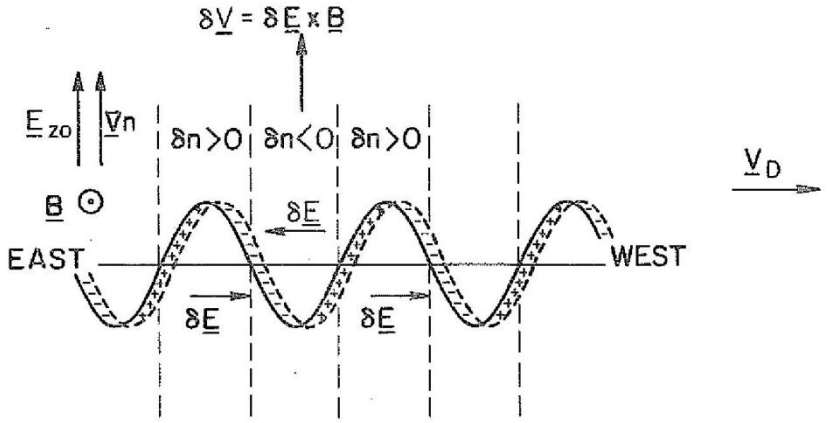

Fig. 4.31. Schematic diagrams showing the linear instability mechanism in (a) the two-stream process for nighttime conditions and (b) the gradient drift process for daytime conditions.

Mid-latitude E-region FAI

Earlier observations with the MU radar (Shigaraki, Japan)

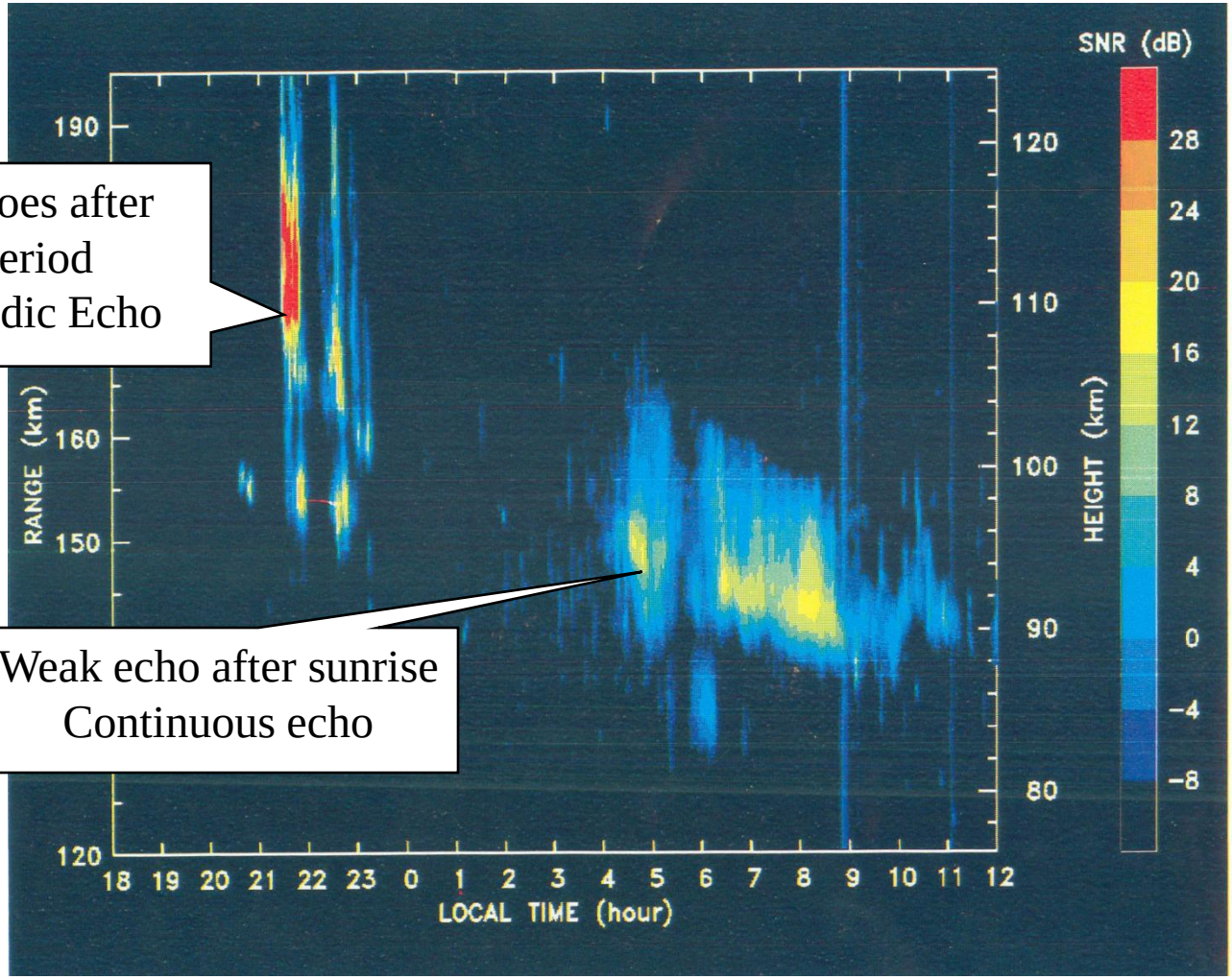

Intense echoes after sunset period Quasi-Periodic Echo

Weak echo after sunrise Continuous echo

Yamamoto et al., 1991

Mid-latitude E-region FAI

Earlier observations with the MU radar (Shigaraki, Japan)

Close-up of evening echoes

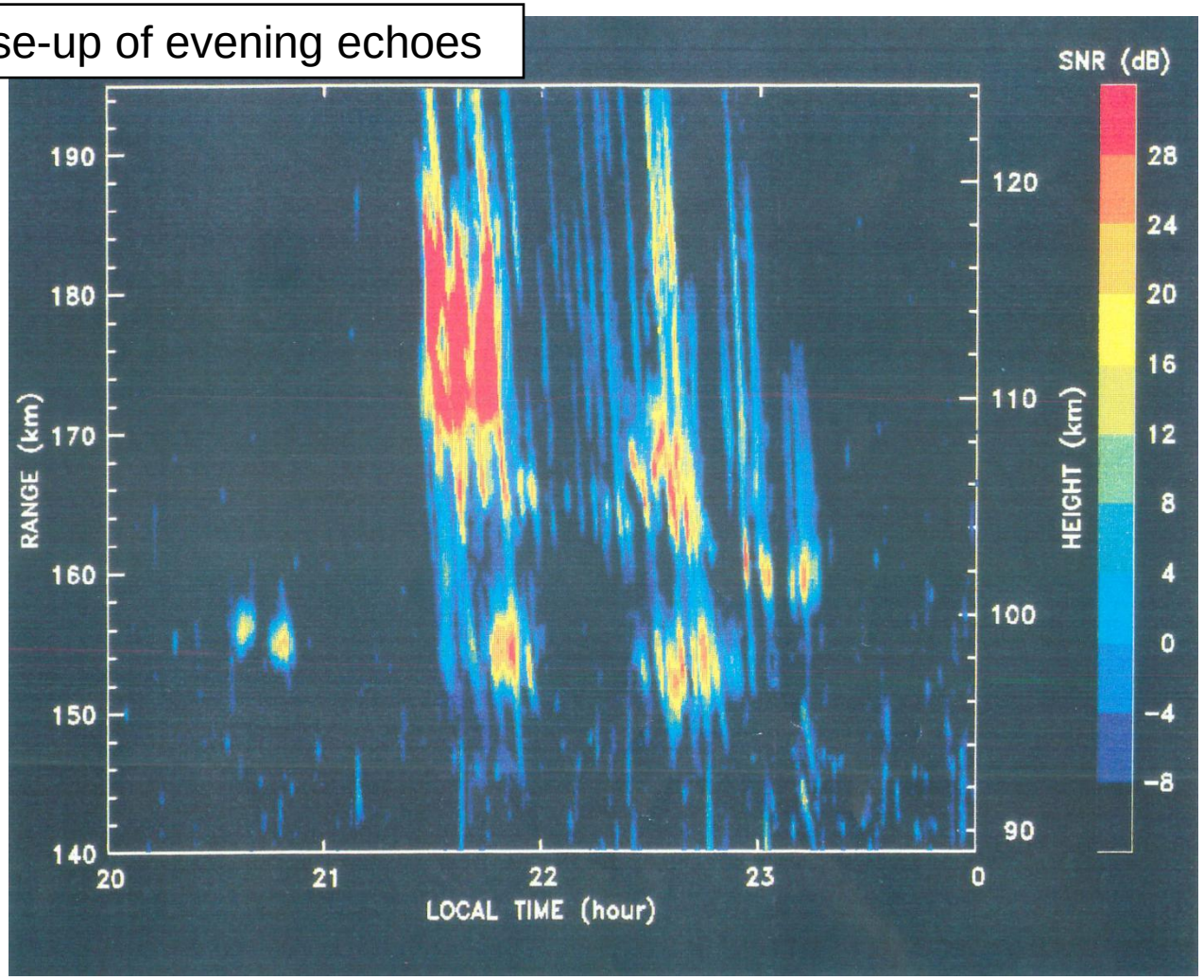

Yamamoto et al., 1991

Horizontal structure of mid-latitude E-region FAI

MU radar + Frequency Agile Radar simultaneous obs.

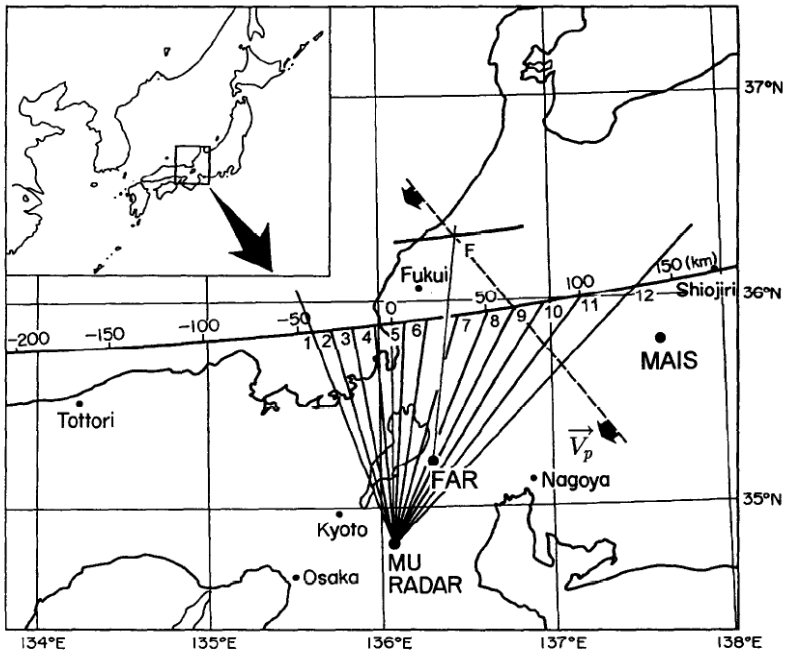

Fig. 1. Observation areas of cooperative observations of *E* region field-aligned irregularities between the MU radar (MUR) and the Frequency Agile radar (FAR). The long zonal line designates the region where the antenna beam of the MUR is perpendicular to the geomagnetic field at the altitude of 100 km. Observation areas for 12-beam observations of the MUR are distributed along the line as shown by the numbers '1'–'12'. The observation area of the FAR is shown by the point 'F'. The Multicolor Airglow Imaging System (MAIS) from Tohoku University is located at the Kiso observatory as shown in the figure.

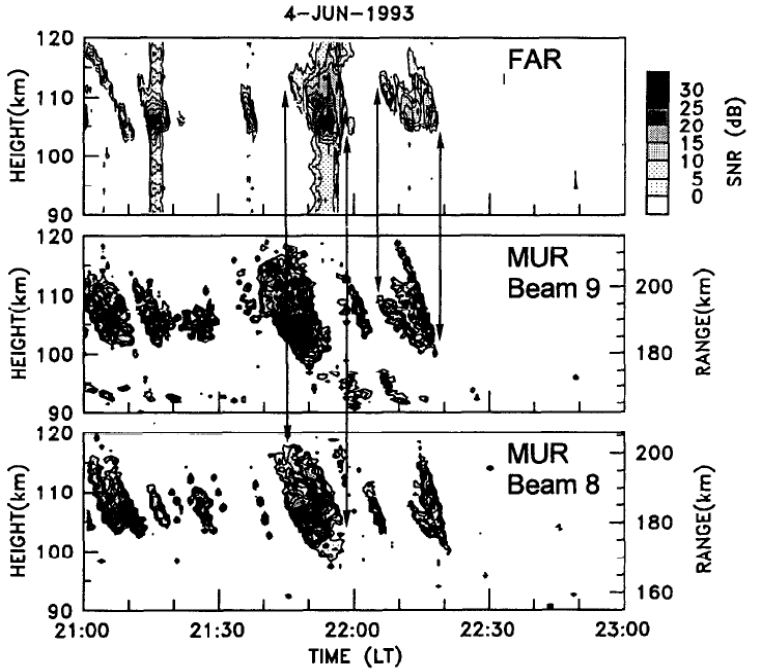

Fig. 3. Range Time Intensity (RTI) plots of FAI echoes observed during 21–23 LT (LT = UT + 9 h) on 4 June 1993 within the FAR beam (top panel), and in the beams 8 (middle panel) and 9 (bottom panel) of the MUR. The intensity is shown by the signal-to-noise ratio (SNR). The altitude of the echoes is determined by assuming that they appear from a direction which is perpendicular to the geomagnetic field as determined from the IGRF85 model. Note that the FAR data appear 2 km higher than the MUR ones because of possible additional system delay. In the FAR data at around 21:16 and 21:53 LT, vertically extended echoes appeared as a result of range sidelobes of the 13-bit Barker coded pulse.

Yamamoto et al., 1997

F-region Medium-Scale Traveling Ionospheric Disturbance (MSTID)

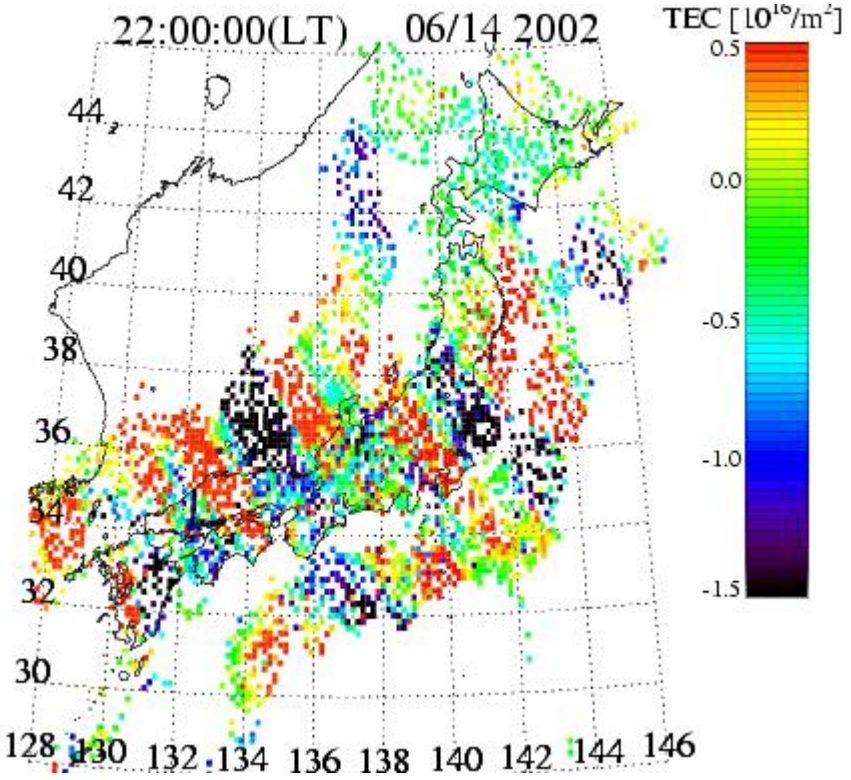

GPS-TEC over Japan

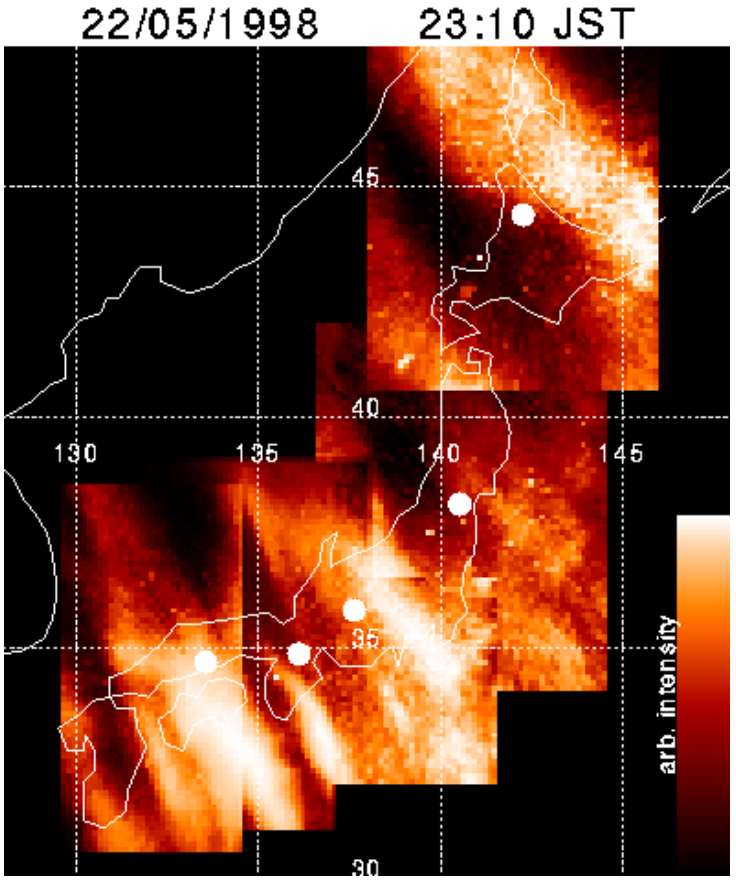

Red airglow (630nm) over Japan

Summary

- Ionosphere Irregularity
  - Irregularities are driven by polarization electric filed that arises from plasma-density variation & current continuity.
  - Large range of scales: several meters to 100km.
- ESF or plasma bubble
  - Occur after equatorial F-region sunset. Also generated by magnetic storms
  - Understood by R-T instability, but seeding mechanism is not fully understood.
- E-region FAI
  - Type 1 and 2 instabilities are well known. Type 2 are seen in the mid-latitude region.
- Coupling with the neutral atmosphere
  - Vertical coupling of the Earth's atmosphere is important.

Equatorial electrojet

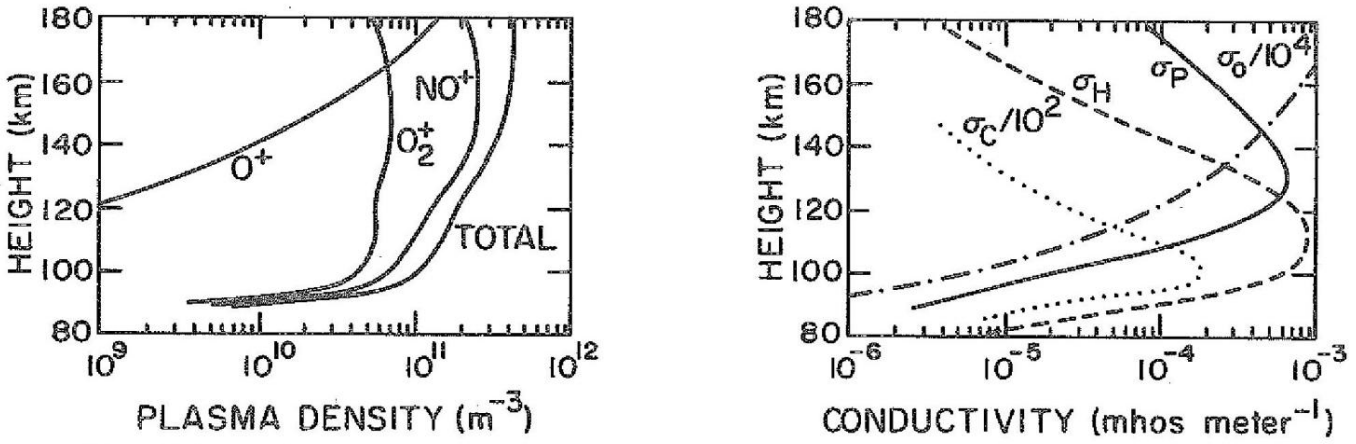

Fig. 3.14. Vertical profiles of daytime composition and plasma density (left) and conductivities (right) for average solar conditions. [After Forbes and Lindzen (1976). Reproduced by permission of Pergamon Press.]

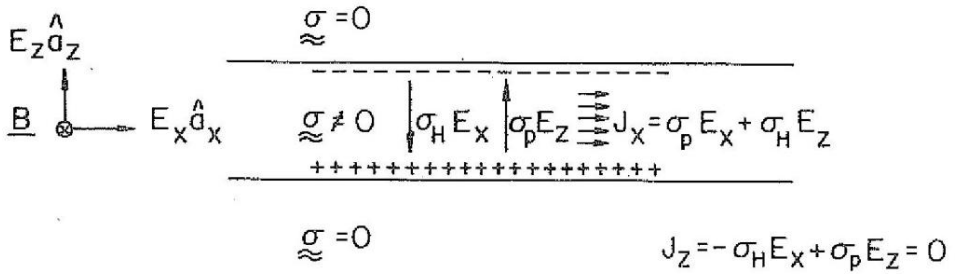

Fig. 3.15. The equatorial electrojet in a slab geometry.

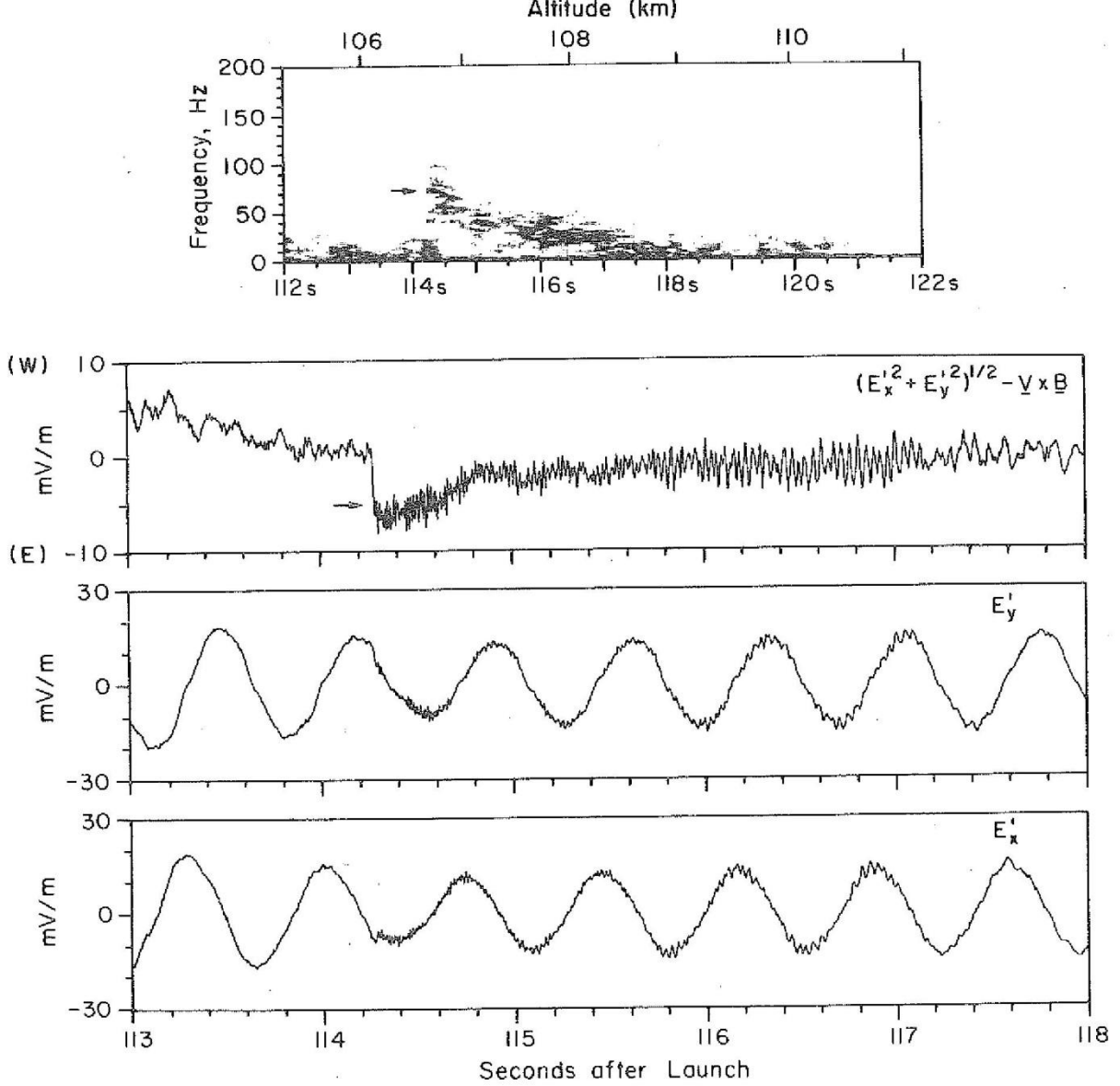

Fig. 4.29. Electric field observations of the two-stream waves for the upleg. The lower panels show the raw dc-coupled data, above which is plotted the square root of the sum of the squares of these waveforms. The upper panel shows a sonogram of these waves. (Note the change in scale of the time axis.) An arrow indicates the onset of the strong burst of primary two-stream waves. [After Pfaff *et al.* (1988b). Reproduced with permission of the American Geophysical Union.]

Figure title

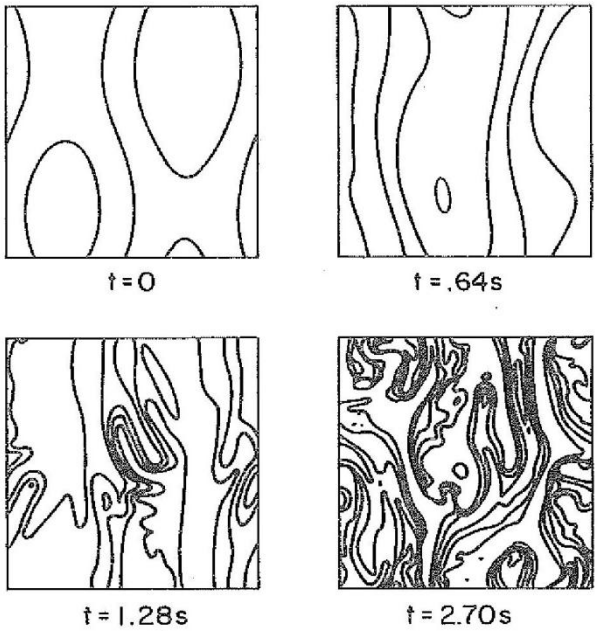

Fig. 4.35. Plasma density contours showing the development of the equatorial irregularities at four selected times. The contour spacing is 2.5% of the ambient density, and the grid spacing is 1.5 m. [After McDonald *et al.* (1975). Reproduced with permission of the American Geophysical Union.]

E-region FAI experiment with MU radar

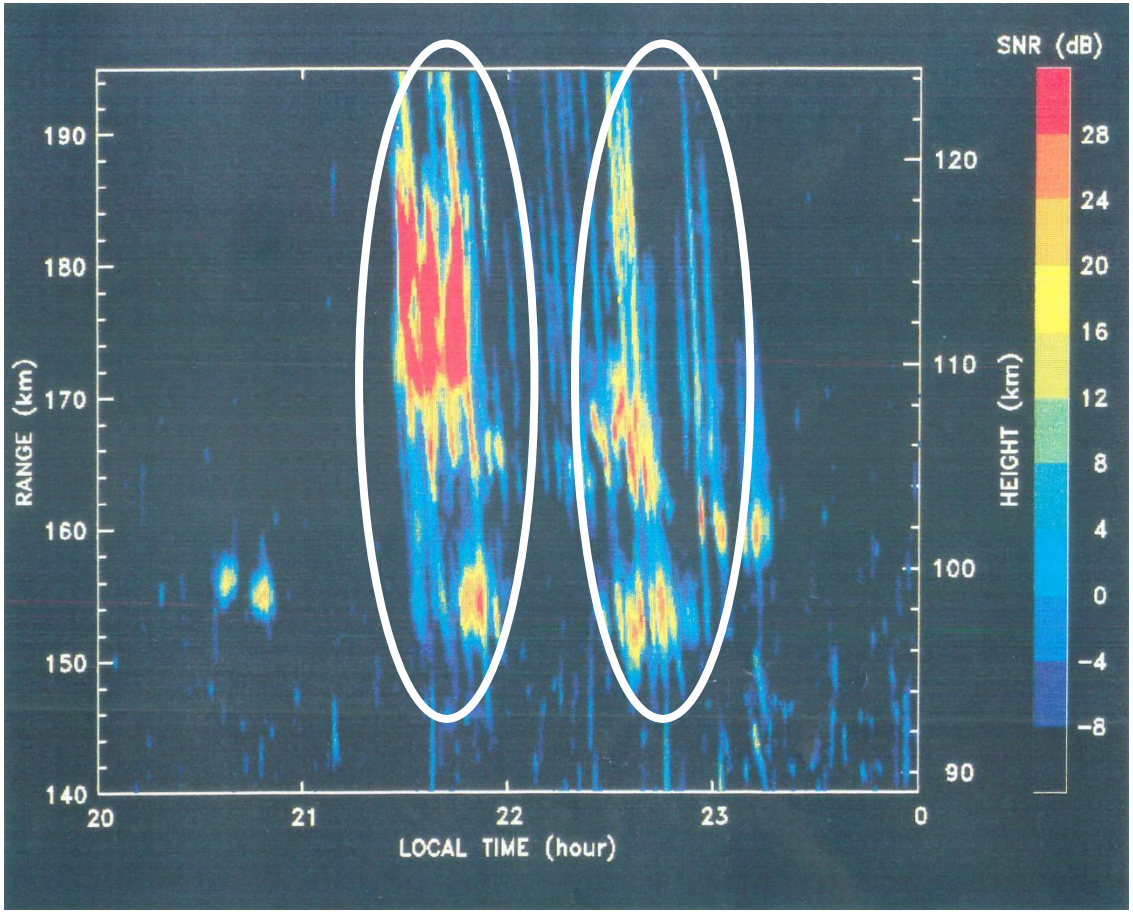

- QP echoes (several minutes) appear after summer sunset period.
- Echo enhancements look to have slower variation of about ~1 hour.

Yamamoto et al., 1991

Equatorial Atmosphere Radar (EAR)

Antenna field (110m in diameter)

Location:
Kototabang,
West Sumatra,
Indonesia
(0.20° S, 100.32° E)

100 kW, 560 Yagi antennas

Interactions between the Lower and Upper Atmosphere over the Equatorial Region

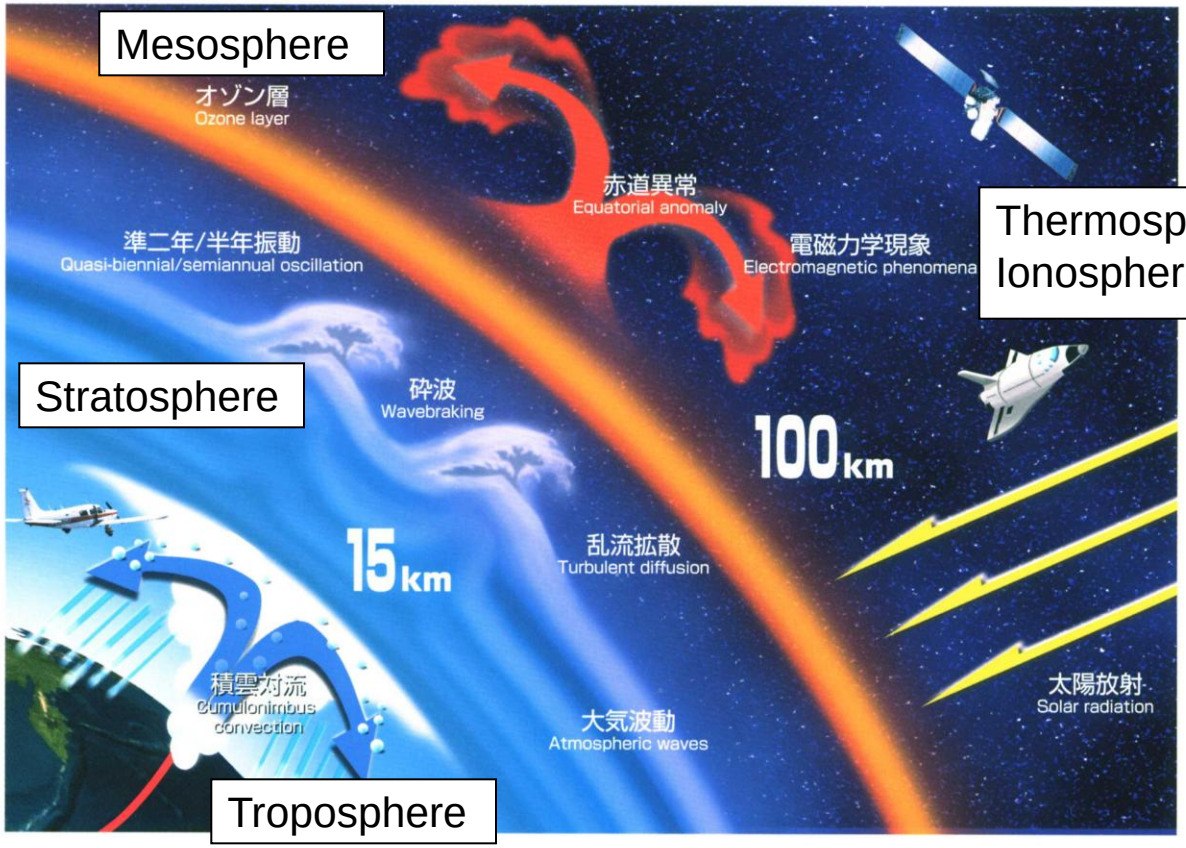

▲ 赤道大気の諸現象
Phenomena in the equatorial atmosphere

The equatorial atmosphere featured by :

- ✧Maximum input of solar radiation
- ✧Minimum Coriolis effect
- ✧Horizontal geomagnetic field

CPEA
赤道大気上下結合

Interactions between the Lower and Upper Atmosphere over the Equatorial Region

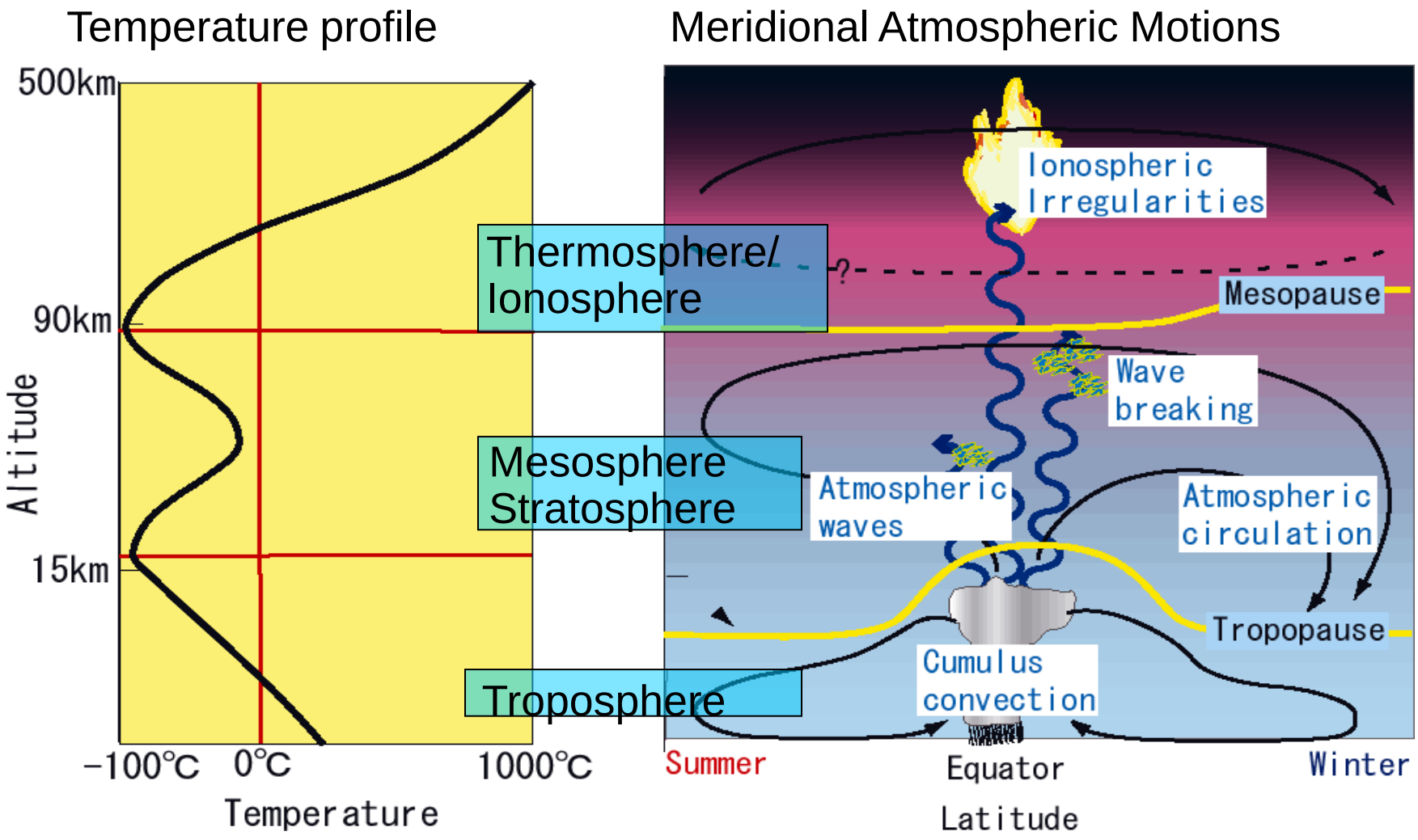

EAR long-period experiment

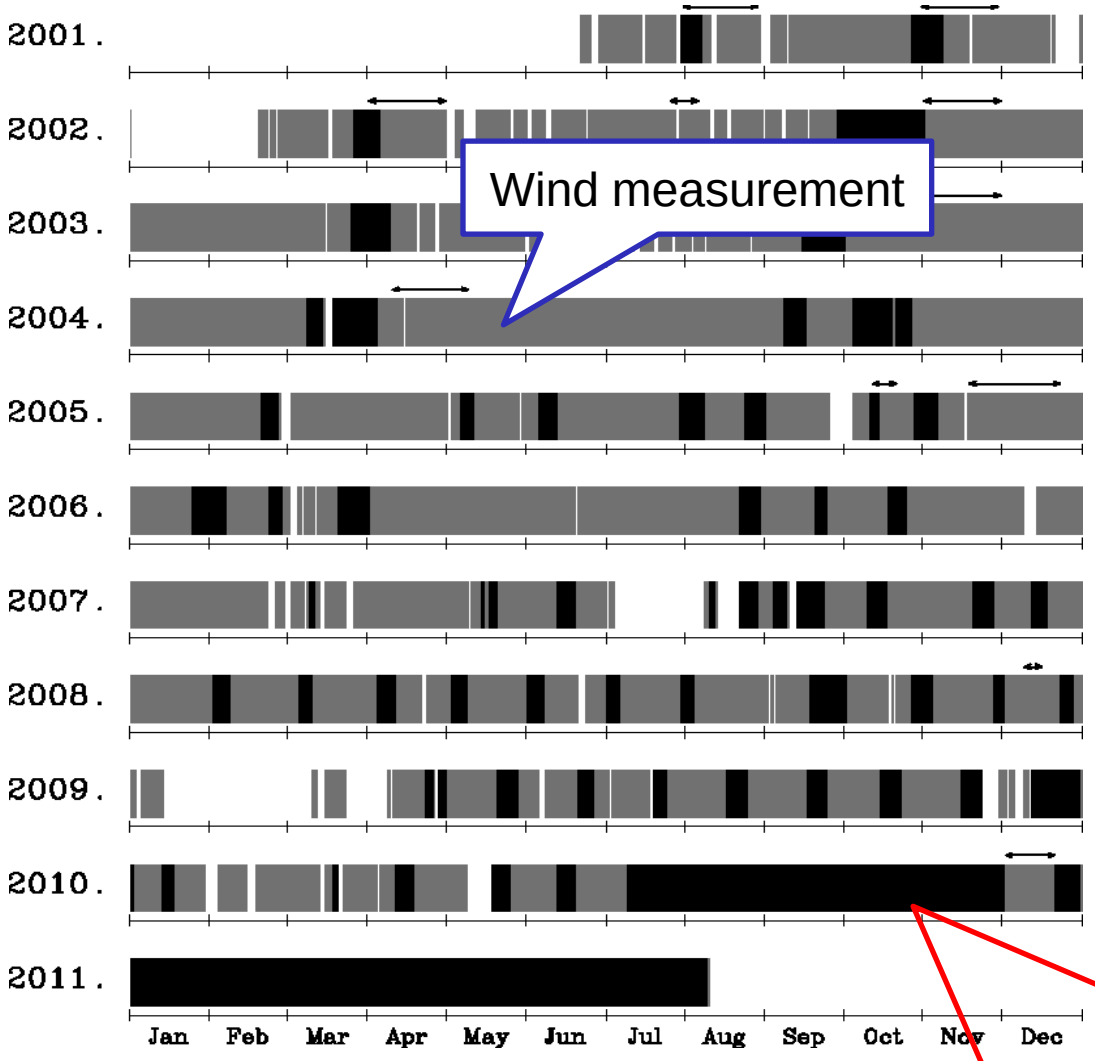

EAR continues long-period continuous observations since June 2001. Most of them were for wind measurement of the troposphere and stratosphere.

From July 2010, we shift the observation mode to more ionosphere studies owing to the current research program of “Indonesia Space Weather”

Continuous ionosphere measurement started in July 2010

Large Scale Wave Structure (LSWS)

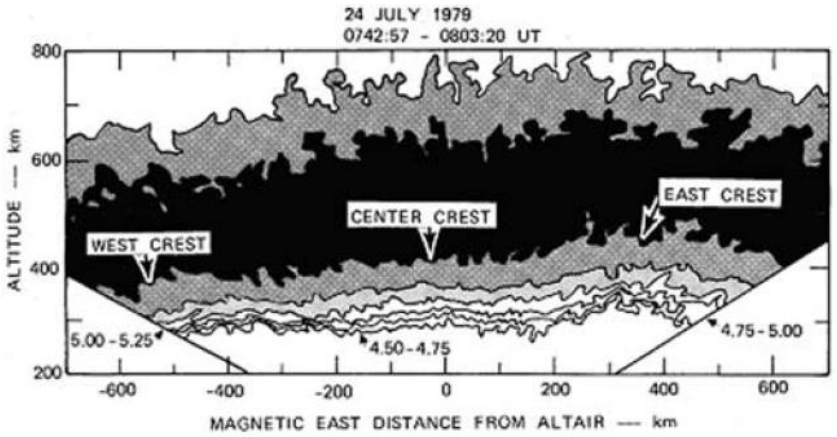

Figure 1. Plasma-density distribution measured during an east-to-west scan with the ALTAIR incoherent-scatter radar, on 24 July 1979 between 0742:57 and 0803:20 UT [from *Tsunoda and White*, 1981].

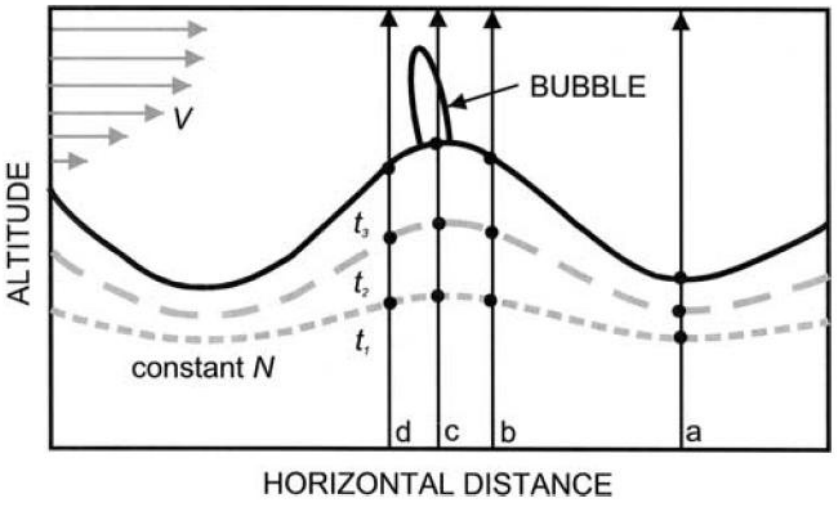

Figure 3. Sketch showing amplification of wave structure and overhead measurements from four locations, labeled a, b, c, and d.

LSWS: Zonal structure of ionosphere with wavelength of ~500km

←→ Show good correlation with ESF event

○ Plasma irregularity is proposed to support growth of LSWS.

○ Observations are still very limited.

Tsunoda et al, 2005

Longitudinal distribution of ESF

Fukao et al., 2006

Case study on March 24, 2004

Four regions of ESF (A、B、C、D) were observed during 20-0 LT

Spatial interval between ESF A-D

Distance：~ 500 km in average

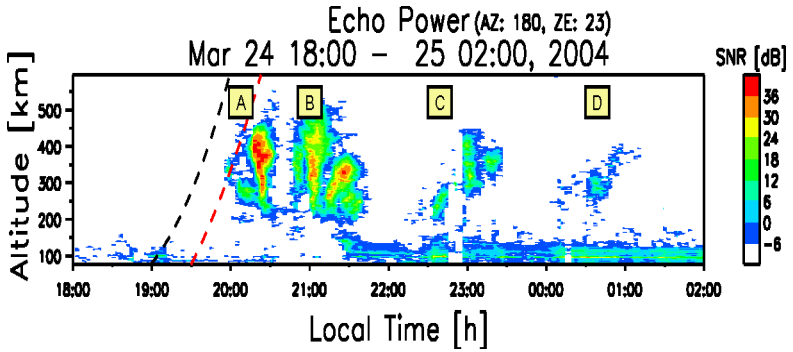

Typical interval between ESF clusters (16 cases)

Average：690 km (S.D.：180 km)

Minimum：370 km

Maximum：1000 km

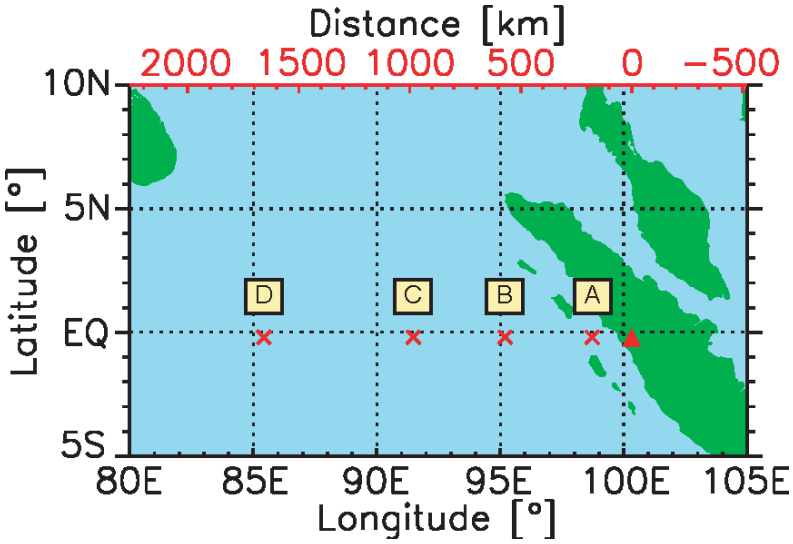

Possible modulation of ESF owing to gravity waves.

Onset time and altitude range of ESF echoes

Yokoyama et al., 2004

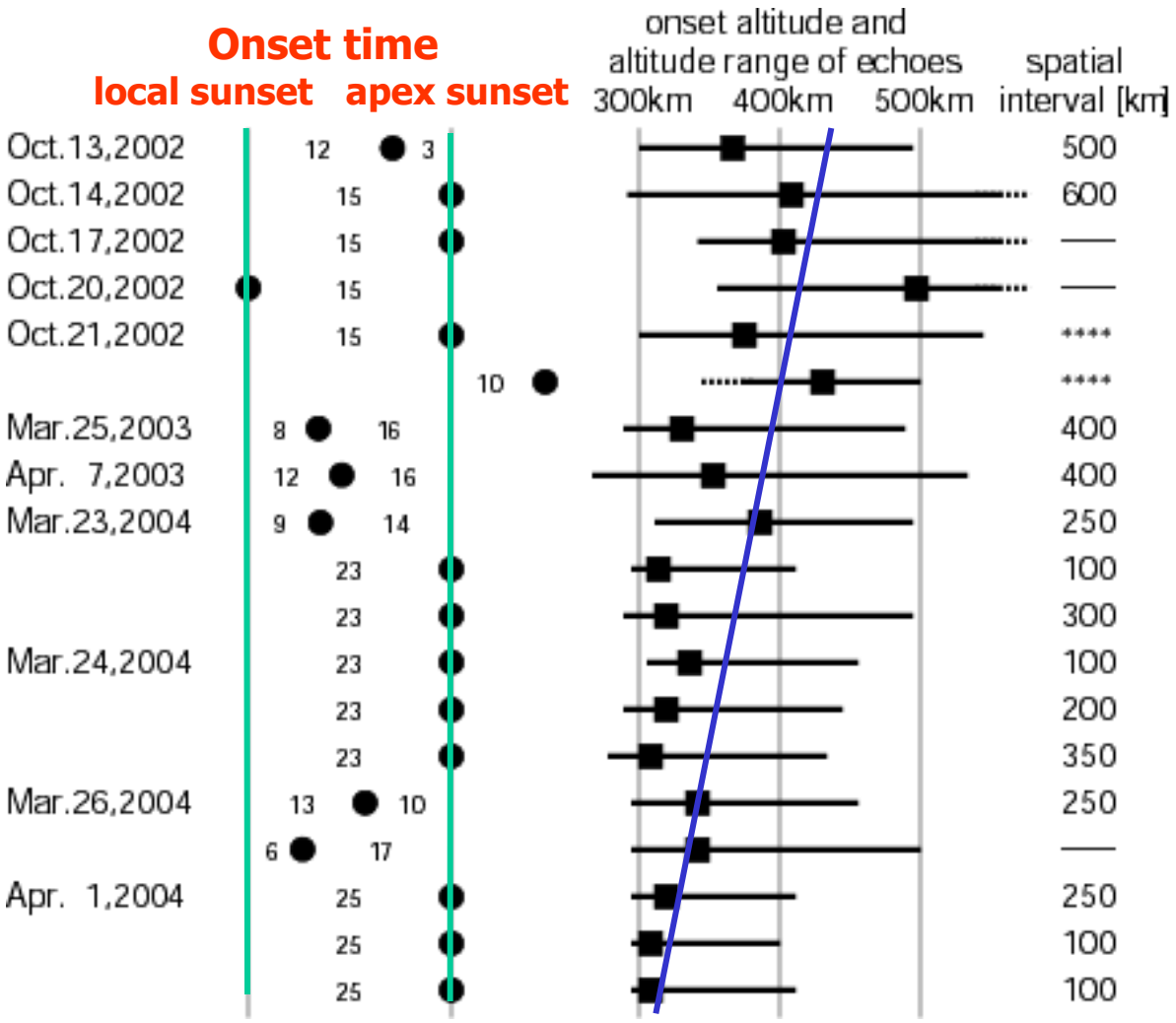

19 out of ~80 plumes were born within the fan sector